Monotonic solution of flow and transport problems in heterogeneous media using Delaunay unstructured triangular meshes

Costanza Aricò *, Marco Sinagra, Tullio Tucciarelli

Dipartimento di Ingegneria Civile, Ambientale, Aerospaziale, dei Materiali, Università di Palermo, Viale delle Scienze, 90128 Palermo, Italy

ABSTRACT

Transport problems occurring in porous media and including convection, diffusion and chemical reactions, can be well represented by systems of Partial Differential Equations. In this paper, a numerical procedure is proposed for the fast and robust solution of flow and transport problems in 2D heterogeneous saturated media. The governing equations are spatially discretized with unstructured triangular meshes that must satisfy the Delaunay condition. The solution of the flow problem is split from the solution of the transport problem and it is obtained with an approach similar to the Mixed Hybrid Finite Elements method, that always guarantees the *M*-property of the resulting linear system. The transport problem is solved applying a prediction/correction procedure. The prediction step analytically solves the convective/reactive components in the context of a MAST Finite Volume scheme. The correction step computes the anisotropic diffusive components in the context of a recently proposed Finite Elements scheme. Massa balance is locally and globally satisfied in all the solution steps. Convergence order and computational costs are investigated and model results are compared with literature ones.

© 2012 Elsevier Ltd. All rights reserved.

1. Introduction

There are several numerical difficulties which must be addressed when solving transport equations, occurring in porous media and including convection, diffusion and chemical reactions processes. These problems include, for example, the approximation of sharp fronts, grid orientation effects and, for reactive processes in particular, different time-scales.

Anisotropy is the tendency of a transport phenomenon to align progressively along preferential directions. Diffusion equation with anisotropic coefficients arises in many environmental topics, for example heat transfer, groundwater flow and transport problems, petroleum reservoir simulations, hydrodynamic simulations,... In groundwater contaminant transport problems, principal directions of the diffusive tensor, representing mechanical dispersion, are the same velocity direction and other two directions lying in the normal plane. Velocity fields varying in space and time cause (possibly sharp) changes of the anisotropy directions. These problems are characterized by a full rank diffusion tensor, that is diagonal only if the reference system is aligned with the principal anisotropy directions [5]. The anisotropy ratio is the ratio between the largest and the smallest tensor eigenvalue.

Many numerical solvers proposed for the solution of anisotropic diffusion problems have shown difficulties in satisfying the Discrete Maximum Principle (DMP), that guarantees asymptotic solutions free of oscillations and monotonic in space ([28] and cited references). In addition, mesh locking effects may arise for strong anisotropy problems, when the spatial rate of convergence decreases along with the increment of the anisotropy ratio [21,22].

Many numerical methods proposed in literature for the solution of general transport problems originate from the splitting of the original flux into advective and diffusive components and different Partial Differential Equations (PDEs) systems solve only one of the two terms. Each PDEs system is discretized in space and time with a different technique, deemed to be the most appropriate for the specific component. Most often, explicit time-stepping for advective fluxes are combined with implicit time-stepping for diffusive fluxes. Eulerian–Lagrangian schemes [10,31] and Eulerian–Godunov schemes [14,15] belong to these kinds of splitting methods. Characteristic methods solve separately for advection and diffusion, using a Lagrangian treatment of the advective part and an Eulerian treatment on the fixed grid of the diffusive part of the transport equation. In general, these methods do not conserve mass and fail to treat boundaries in a straightforward manner. Celia et al. [12] and Healy and Russel [23] introduced an improved characteristic method called the Eulerian–Lagrangian localized adjoint method (ELLAM) which uses space–time test functions that are carried through space and time by the

* Corresponding author.
  E-mail addresses: costanza.arico@unipa.it, arico@idra.unipa.it (C. Aricò), marco.sinagra@unipa.it (M. Sinagra), tullio.tucciarelli@unipa.it (T. Tucciarelli).

characteristics of the velocity field. ELLAM ensures mass conservation in a global sense and allows for systematic treatment of inflow and outflow boundaries. Since these schemes solve the advective part of the transport problem by tracking particles along the characteristics, Eulerian–Lagrangian schemes are suitable to solve transport problems in cases of simple flow fields ad homogeneous permeability medium. Smooth Particle Hydrodynamics (SPH) is a novel techniques that is part of the so called meshless methods. Meshless methods compute the concentration within domain where the velocity field is known and the concentration solution is represented in space and time as function of the concentration and location of a fixed number of particles moving in the domain [25]. These methodologies have successfully applied to isotropic diffusion transport problems, but their use in the simulations of anisotropic problems is an ongoing research activity [25].

An efficient strategy for the numerical simulation of phenomena where both convection and diffusion effects are significant, consists also in coupling Finite Volumes (FV) schemes with Finite Elements (FE) schemes.

In recent years, strong attention has been given to higher-order Godunov techniques for advective flow problems. Dawson [15] investigated the combination of these techniques with Mixed Finite Elements (MFE) methods for advection-dominated equations. The author refers to this general approach as the Godunov-mixed method (GMM). The combination of these two schemes is natural because both are based on a weak form of the differential equations and assume discontinuous trial functions.

The GMM has been extended by Mazzia et al. [29] to unstructured triangular grids and by Mazzia et al. [30] to 2D and 3D transport problems in porous media. For the advective components of the transport equation, the authors in [29,30] adopt high resolution triangular FV discretization, combined with an implicit Mixed Hybrid Finite Elements (MHFE) scheme for the solution of the flow equation and of the diffusive components in the transport equation. MHFE methods compute a velocity field which is very convenient for the solution of the next convective transport problem with the FV methods, since the normal velocity components are continuous across the inter-element boundaries. This avoids mass balance errors in the solution of the transport equations due to inaccuracies in the evaluation of the fluxes through the element interfaces. In addition, the use of a dual mesh for the FV scheme is not necessary if a MHFE method is applied for the discretization of the diffusive components.

Because of the explicit time discretization, most often the solution of the advective components is limited by the Courant (CFL) stability requirement on the size of the time step, while, because of the implicit time discretization, there is no restriction on the time step of the MHFE. This implies that different time steps are often used for the solution of the advection and of the diffusion problems. Solution of the advective components is carried out by applying na times the FV scheme using a time step size $\Delta ta = \Delta t/na$. Values of na and Δta vary inside the computational domain according to the CFL restriction.

GMM has been applied successfully to the solution of density dependent flow and transport problems, characterized by convective recirculating flows originated by density buoyancy forces. Applications to benchmark test problems in 2D and 3D ([30] and cited references) have assessed the accuracy and reliability of this numerical approach. This combination of mixed Finite Elements methods and shock-capturing methods was also proved successful in the numerical treatment of models involving systems of equations of different nature, such as those encountered in groundwater flow and reactive transport of contaminants [18,19].

Herbin and Hubert [24] presented a review of several numerical schemes developed for the treatment of anisotropic diffusion problems. Most of these schemes, like the MHFE or the compact stencil Multi Point Flux Approximation (MPFA) schemes, are naturally suited for coupling with FV-bases convective solver, as they use the same cell-centred unknowns.

Some numerical experiments concerning anisotropic heterogeneous diffusion problems (see for example [20]) have shown that, for high anisotropy ratios, some MPFA fail to converge when applied to highly refined computational meshes and some MHFE compute unphysical oscillations.

Recently, Mazzia et al. [30] examined the behavior and the efficiency of the GMM technique, when applied to strongly anisotropic problems. At increasing anisotropy ratios GMM suffers from increasing ill-conditioning and spurious oscillations may appear in the numerical approximation of the time-dependent solution. These oscillations may be hidden from the numerical solution as a result of the application of the flux limiter that is employed in the FV solver due to the hyperbolic character of the convective term. This aspect makes this problem even more subtle and difficult to spot, thus increasing the chances to confuse it with a real physical behavior when complex problems are tackled.

Substitution of the MHFE discretization in GMM with a standard linear ($P1$) Galerkin method, leads to sensibly different numerical concentration fields, without the flaw of spurious oscillations [30]. This latter approach is referred to as the Godunov-$P1$ Method (G-$P1$ M). Resolving system of the G-$P1$ M has a much better spectral condition number (much closer to one) than the GMM system. G-$P1$ M does not show any mesh locking effect for the range of the anisotropy ratios which are typical of groundwater transport problems [30].

The main drawback in the use of the G-$P1$ M method is that the coupling of node-based methods, such as $P1$ Galerkin, with the Godunov FV requires interpolation between nodal and cell values and viceversa [30].

The MFE methods have provided an attractive framework for the solution of potential flow problems, like groundwater flow simulations: by simultaneously approximating the potentials and the normal fluxes, the computed normal fluxes are continuous across inter-element edges and the local and global mass balance are automatically achieved in the case of constant parameters. MFE methods have been extensively used for the solution of parabolic problem, but in elliptic problems (i.e. steady state problems) the matrix of the system becomes ill-conditioned, leading to saddle-point problem [7,26]. Hybridized formulation of MFE, MHFE methods represent a way to solve this problem. In the MHFE method, piezometric heads at element edges are assumed as additional variables to overcome this problem. The final linear algebraic systems are always symmetric and positive definite.

Hoteit et al. [26] proved that in heterogeneous media, the conditioning of the resulting linear system for the MHFE grows up linearly according to the ratio between the highest and the lowest values of the hydraulic conductivity of adjacent elements and the algorithm could accumulate numerical errors if large jumps in the conductivity values take place.

Recently, two lumped Finite Volume formulation of the MHFE scheme have been proposed [35], an edge centred and a cell centred formulation. In the first one, the flow equations are spatially discretized in a set of continuity equations across all the edges of the mesh, using the average potentials along these edges as unknowns. The formulation leads to final linear algebraic systems that are always symmetric and positive definite. In the cell centred formulation, flow equations are discretized over the mesh elements and uses the potential in the cell circumcenter as unknowns. The dimension of the solution system is equal to the elements number, much less than the one of the first lumped formulation, equal to the number of elements edges.

Edge centred formulation leads to an M-stiffness matrix for acute triangulation, for homogeneous or heterogeneous domains,

while the second lumped formulation leads to an *M*-matrix for a Delaunay triangulation in the case of an homogenous domain only. An *M*-matrix is a matrix with diagonal positive coefficients, strictly diagonally dominant, or weakly diagonally dominant with strict inequality for at least one row and non-positive extra-diagonal coefficients. In the numerical solution of second-order PDEs, the *M*-stiffness matrix system prevents from unphysical oscillation (see for example [28,32]).

In heterogeneous domains, the criterion to obtain an *M*-matrix with cell centred formulation depends not only on the geometry but also on the distribution of the permeability medium and the stiffness matrix could not be necessarily positive definite, contrarily to the first lumped formulation and to standard MHFE. This condition is very important when using iterative solvers. Moreover, stiffness matrix of the cell centred formulation can be singular for triangles having one right angle [35].

In the present paper a numerical procedure is proposed for the solution of heterogeneous isotropic flow field and heterogeneous convection–diffusion–reaction transport problems with diffusive anisotropic tensor in saturated porous media. The governing PDEs system is given by the mass conservation equation of the fluid phase, by the Darcy formula for the velocity and by the transport equations of the scalar transported species.

The governing equations are discretized over a generally unstructured triangular mesh, that attains the Generalized Delaunay condition, further defined. Flow field is assumed to be not affected by the concentration field and it is solved at the beginning of each time step. The computed velocity field is second order accurate in space and continuous along the element edges. The algorithm is similar to the cell centred lumped FV-MHFE scheme [35], but includes substantial changes that allows fast and monotonic solutions also using strongly unstructured meshes with obtuse triangles.

Once flow field is known for the given time step, the transport problem is computed by solving consecutively a prediction and a correction problem. The prediction problem, including the convective and the reaction components, is solved by applying the FV Marching in Space and Time (MAST) scheme, previously proposed by some of the authors for the solution of purely convective transport problem [4,1], and here extended to problems where chemical reactions occur. This scheme computes an analytical solution of the element nodal concentration values. Unlike the ELLAM schemes, this method is locally and globally mass conservative for any computed flow field and the mean computational effort per element does not increase with the CFL number [4,1].

The correction step solves the diffusive anisotropic problem according to a recently developed node-based technique [3], where the control volume is the closed polygon given by the union of the midpoint of each side with the "anisotropic" circumcenter of each triangle. The structure of the diffusive flux across the control volume sides is similar to the one of the standard *P*1 Galerkin scheme. A special treatment of the diffusive flux across the dual volumes edges is also proposed in order to guarantee monotonic asymptotic solutions and a positive definite matrix of the final linear system. This treatment requires, if necessary, some edge swaps of the basic mesh triangles, but it does not change the location of the original nodes and also maintains both the internal and the external boundaries. The solver of the anisotropic diffusive transport has shown a spectral condition number much closer to one than the standard *P*1 Galerkin FE scheme (that already has a much better stiffness matrix conditioning than the GMM methods, as proved in [30]), satisfies the DMP and no mesh locking effects have been observed, also for strong anisotropy ratios [3]. Unlike methodology proposed in [3], in the present paper, coefficients of the diffusion tensor change in time, depending on the flow field, as shown in the next section.

The paper is organized as follows. In Section 2 the governing equations are shown, along with the initial and boundary conditions and the physical assumptions. In Section 3, the numerical procedure for the computation of the flow field is presented. Transport problem solution is described in Section 4. Finally, in Section 5 numerical tests are proposed. Computed results are compared with the corresponding ones provided by other literature models; the convergence order and the required computational costs are investigated.

2. Physical assumptions and governing equations

The medium is assumed to be saturated by a single liquid phase, with one chemical soluble species, characterized by its concentration C.

The governing equations for the mass transport in saturated porous media form a non linear PDEs system, given by the flow equation and by the transport equations of the contaminant phase [16].

Let Ω be a physical domain in $\mathbb{R}^2$ (vertical or horizontal plane), Γ the boundary of Ω and $\mathbf{x} = [x_1, x_2]^T$ the spatial co-ordinate vector. Let $H^1(\Omega)$ be the Sobolev space of square-integrable functions with square-integrable first order derivatives over Ω.

The flow equation is:

$$s_0 \frac{\partial H}{\partial t} + \nabla \cdot \mathbf{q} = f_H \quad \text{in} \quad \Omega \times [0, T], \tag{1}$$

where t is time, T is the total simulation time, $H \in H^1(\Omega)$ is the piezometric head (or hydraulic head or potential), s_0 is a storage coefficient, $f_H = f_H(\mathbf{x}, t) \in L_2(\Omega)$ is a source term and $\mathbf{q}$ is the Darcy flow velocity:

$$\mathbf{q} = -\mathbf{K}\nabla H, \tag{2}$$

where $\mathbf{K}$ is the permeability tensor, assumed isotropic, such that $\mathbf{K} \equiv K$ (a positive scalar value). The transport equation for the contaminant phase is:

$$R\varepsilon \left(\frac{\partial C}{\partial t} + \lambda C \right) + \nabla \cdot (\mathbf{q}C) - \nabla \cdot (\mathbf{D}\nabla C) = f_C \quad \text{in} \quad \Omega \times [0, T], \tag{3}$$

where $C \in H^1(\Omega)$ is the mass concentration of the solute component, ε is the effective porosity of the medium, R is the latency retardation factor ($R\varepsilon$ is assumed constant in time), λ is the chemical decay rate ($\lambda = \log 2/T_l$ with T_l the half life of the element), $f_C = f_C(\mathbf{x}, t) \in L_2(\Omega)$ is the sink/source of the solute component and $\mathbf{D}$ is a generally anisotropic diffusion tensor. The unknowns of the problem are the piezometric head H and the contaminant concentration C. To close the set of the governing Eqs. (1) and (3) some constitutive relationship are needed: tensor $\mathbf{D}$ is given by (see for example [5]):

$$\mathbf{D} = (D_d + \alpha_T |\mathbf{q}|)\mathbf{I} + (\alpha_L - \alpha_T) \frac{\mathbf{q} \otimes \mathbf{q}}{|\mathbf{q}|}, \tag{4}$$

where D_d is the effective molecular diffusion coefficient of the fluid, α_L and α_T are the longitudinal and transverse coefficients of the solute dispersivity, $|\mathbf{q}|$ is the absolute specific Darcy fluid flux.

The set of governing PDEs (1) and (3) is subject to the following initial and boundary conditions:

$$\begin{cases} H(\mathbf{x}, 0) = H_0(\mathbf{x}) & \text{in } \Omega \text{ at } t = 0 \ \mathbf{x} \in \Omega, \\ H = H_D(\mathbf{x}, t) \ \mathbf{x} \in \Gamma_D^H \quad \mathbf{q}(\mathbf{x}, t) \cdot \mathbf{n} = g_N(\mathbf{x}, t) \ \mathbf{x} \in \Gamma_N^H, \end{cases} \tag{5, a}$$

as well as

$$\begin{cases} C(\mathbf{x}, 0) = C_0(\mathbf{x}) & \text{in } \Omega \text{ at } t = 0 \ \mathbf{x} \in \Omega, \\ C = C_D(\mathbf{x}, t) \ \mathbf{x} \in \Gamma_D^C \quad C\mathbf{q}(\mathbf{x}, t) \cdot \mathbf{n} = g_N^C(\mathbf{x}, t) \ \mathbf{x} \in \Gamma_N^C, \end{cases} \tag{5, b}$$

where $\Gamma_D^{H(C)}$ and $\Gamma_N^{H(C)}$ are the portions of boundary Γ where Dirichlet and Neumann conditions respectively hold for $H(C)$, sub index

"0" marks the initial states for H and C, H_D and C_D are the Dirichlet values for H and C on Γ_D^H and Γ_D^C respectively, g_N is the assigned Neumann flux on Γ_N^H ($\mathbf{n}$ is the unit outward normal to the boundary) and g_N^C is the assigned Neumann contaminant mass flux on Γ_N^C.

Let Ω_h be a polygonal approximation of Ω, T_h an unstructured triangulation of Ω_h, which properties will be further specified. T_h is called *basic mesh*, N_T is the number of triangles T of T_h. Triangle T is called *primary element*, area of T is $|T|$ and the boundary of T is ∂T. Let $P_h = \{P_i, i = 1,\ldots,N\}$ be the set of all vertices (or nodes) of all $T \in T_h$ with N the number of nodes. A dual mesh $E_h = \{e_i, i = 1,\ldots,N\}$ is constructed over the basic mesh and the dual finite control volume e_i associated with node P_i is the closed polygon given by the union of the midpoint of each side with the "aniso-tropic" circumcenter of each triangle T sharing P_i, as further defined. Dual volumes e_i satisfy:

$$\Omega = \bigcup e_i. \tag{6}$$

Flow field problem and the convective/reaction components of the transport problem are solved over a basic mesh and the computational cell is the mesh triangle itself, while the diffusive component of the transport problem is solved over a different dual mesh, sharing the same nodes of the previous one, and the computational cell is the dual control volume.

3. Flow field solution

In the context of MHFE formulation [35], solution of problem (1) is approximated inside triangle T_m by the following quantities: H_m, the mean value of the piezometric head in T_m, $\mathbf{q}^m \in RT_0$ (RT_0 is the Raviart–Thomas lowest order space over T_m [33]), approximation of $\mathbf{q}$ over T_m and the values Tp_j^m ($j = 1, 2, 3$) of the piezometric heads over the three edges of T_m. Flux can be defined element by element as [35]:

$$\mathbf{q}^m = \sum_{j=1,3} \tilde{q}_j^m \mathbf{v}_j^m, \quad m = 1, 2, \ldots, N_T, \tag{7}$$

where $\tilde{q}_j^m$ is the value of the normal flux on edge l_j^m of triangle T_m and the basis functions $\mathbf{v}_j^m$ of $RT_0(T_m)$ are defined as ([35] and cited references):

$$\mathbf{v}_j^m(\mathbf{x}) = \frac{1}{2|T_m|}(\mathbf{x} - \mathbf{x}_j^m), \quad j = 1,2,3, \quad \forall \mathbf{x} \in T_m, \tag{8}$$

where $(\mathbf{x}_j^m)$ are the co-ordinates of the T_m nodes. Important properties of the RT_0 space are ([35] and cited references):

$$\nabla \cdot \mathbf{q}^m \text{ constant on } T_m \quad \mathbf{q}^m \cdot \mathbf{n}_l \text{ constant over each edge}. \tag{9}$$

Call i, ip and im the nodes of triangle T_m, where ip and im are the nodes following and preceding respectively node i in counterclockwise direction. The edge vector $\mathbf{r}_{i,ip}$ ($\mathbf{r}_{i,im}$) connects nodes i and ip (im), oriented from i to ip (im). According to the properties of RT_0 space in Eq. (9), the flux law (2) can be written in variational form as (see also [35]):

$$\int_{T_m} \mathbf{q}^m \cdot \mathbf{v}_i^m = \sum_{j=i,ip,im} \tilde{q}_j^m \int_{T_m} \mathbf{v}_i^m \cdot \mathbf{v}_j^m = \widehat{K_m} \int_{T_m} \nabla H \cdot \mathbf{v}_i^m$$
$$= \widehat{K_m}(\widehat{H_m} - Tp_i^m) \quad i = 1, 2, 3, \tag{10}$$

where symbol $(\widehat{\cdot})$ marks the mean value in the triangle T_m. Eq. (10) can be written as [35]:

$$\tilde{q}_i^m = \widehat{K_m} \sum_{j=i,ip,im} A_{ij}^{-1}(\widehat{H_m} - Tp_j^m), \tag{11}$$

where matrix $A_{ij} = \int_{T_m} \mathbf{v}_i^m \cdot \mathbf{v}_j^m$ is symmetric and positive definite.

Starting from simple algebraic transformations [13,34], it is possible a formulation of the problem with one unknown per ele-

ment. According to Eq. (11), the mixed approximation $\tilde{q}_i^m$ of the flux through side i of element T_m can be written as [35]:

$$\tilde{q}_i^m = -\frac{\widehat{K_m}}{|T_m|}\mathbf{r}_{i,ip}(\mathbf{r}_{i,ip}Tp_{im}^m - \mathbf{r}_{ip,im}Tp_i^m - \mathbf{r}_{im,i}Tp_{ip}^m). \tag{12}$$

Define a new unknown H_m at the circumcenter c_{T_m} of T_m:

$$H_m = \sum_{j=i,ip,im} \pi_j^m Tp_j^m, \tag{13}$$

with coefficient π_i^m given by [34,35]:

$$\pi_i^m = \frac{(\mathbf{r}_{im,ip} \cdot \mathbf{r}_{i,ip})(\mathbf{r}_{im,i} \cdot \mathbf{r}_{ip,i})}{4|T_m|^2}. \tag{14}$$

Eq. (11) becomes:

$$\tilde{q}_i^m = \chi_{i,ip}^m(H_m - Tp_i^m), \tag{15}$$

where coefficient $\chi_{i,ip}^m$ is [34,35]:

$$\chi_{i,ip}^m = -\frac{4\widehat{K_m}|T_m|}{\mathbf{r}_{im,i} \cdot \mathbf{r}_{im,ip}}. \tag{16}$$

Formulation in Eq. (16) of coefficient $\chi_{i,ip}^m$ can be written in the following form:

$$\chi_{i,ip}^m = \frac{\widehat{K_m}}{c_{i,ip}^{T_m}}|\mathbf{r}_{i,ip}|, \tag{17}$$

where $|\mathbf{r}_{i,ip}|$ is the length of side $\mathbf{r}_{i,ip}$ and $c_{i,ip}^{T_m}$ is the distance between the T_m circumcenter ($\mathbf{x}_{c_m}$ its co-ordinate vector) and the midpoint of $\mathbf{r}_{i,ip}$ ($\mathbf{x}_{i,im}$ its co-ordinate vector), written as (see Fig. 1):

$$c_{j,jp}^{T_q} = \frac{(x_{1,j} - x_{1,jp})(x_{2,c_q} - x_{2,jp}) - (x_{2,j} - x_{2,jp})(x_{1,c_q} - x_{1,jjp})}{\sqrt{(x_{1,j} - x_{jp})^2 + (x_{2,j} - x_{2,jp})^2}}\delta_q,$$
$$q = \begin{cases} m \\ e \end{cases} \Rightarrow j = \begin{cases} i \\ im \end{cases}, \quad jp = \begin{cases} im \\ i \end{cases}, \tag{18}$$

where $\mathbf{x}_{j,jp}$ is the co-ordinate vector of midpoint of side $\mathbf{r}_{j,jp}$, $\mathbf{x}_{c_q}$ is the co-ordinate vector of circumcenter of triangle T_q and $\delta_q = -1$ or 1 if direction of vector $\mathbf{r}_{j,jp}$ is respectively counterclockwise or not in triangular element T_q.

Forcing the flux continuity between the two adjacent elements T_m and T_e sharing side $\mathbf{r}_{i,im}$ (oriented from im to i in T_m and from i to im in T_e), is equivalent to set:

$$\tilde{q}_{im}^m = \tilde{q}_i^e = -\tilde{q}_{im}^e = \frac{\chi_{im,i}^m \chi_{i,im}^e}{\chi_{im,i}^m + \chi_{i,im}^e}(H_m - H_e). \tag{19}$$

We get the Finite Volume mass balance equation for the same triangular element by summing the fluxes through the three edges of T_m, that is:
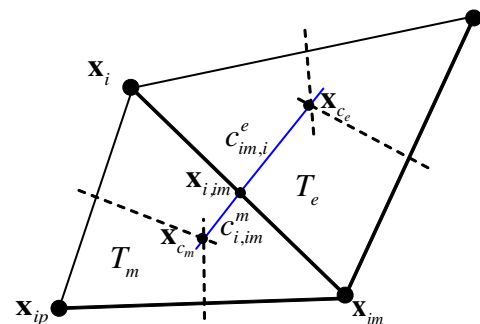

Fig. 1. Triangle notations.

$$|T_m| \widehat{s_{0m}} \frac{\partial H_m}{\partial t} + \sum_j \chi_{j,jp}^{m,e}(H_m - H_e)\delta_j^{m,e} = |T_m|\widehat{f_H^m},$$

$$j = \begin{cases} i \\ ip \\ im \end{cases} \Rightarrow jp = \begin{cases} ip \\ im \\ i, \end{cases} \tag{20}$$

where index e marks the element T_e sharing side $\mathbf{r}_{j,jp}$ with T_m, $\delta_j^{m,e}$ is a Kronecker delta, equal to 1 if T_m shares side $\mathbf{r}_{j,jp}$ with T_e and equal to 0 otherwise and coefficient $\chi_{j,jp}^{m,e}$ is given by:

$$\chi_{j,jp}^{m,e} = \frac{\chi_{j,jp}^m \chi_{jp,j}^e}{\chi_{j,jp}^m + \chi_{jp,j}^e} = \frac{|\mathbf{r}_{j,jp}|}{\left(\frac{c_{j,jp}^{T_m}}{K_m} + \frac{c_{jp,j}^{T_e}}{K_e}\right)} \tag{21}$$

and $c_{jp,j}^{T_e}$ is defined in Eq. (18).

After fully implicit time discretization, Eqs. (20) and (21) form a linear system of order N_T. Diagonal term of the stiffness matrix system corresponding to element T_m is:

$$s_{mm} = \frac{\widehat{s_{0m}} |T_m|}{\Delta t} + \sum_j \chi_{j,jp}^{m,e} \tag{22, a}$$

and its extra-diagonal term corresponding to triangle T_e is:

$$s_{me} = -\chi_{j,jp}^{m,e}. \tag{22, b}$$

The previous formulation is equivalent to the MHFE scheme lumped in the cell center [35]. The drawback of this formulation is that the non oscillatory property, as well as the positive definite property of the resulting linear system are guaranteed only if obtuse triangles are missing and this is very unlike to occur in the real applications.

A Delaunay triangulation in $\mathbb{R}^2$ is defined by the condition that all the nodes in the mesh are not interior to the circles defined by the three nodes of each triangle, as shown in Fig. 2(a) [27]. It can be shown [32] that each Delaunay triangulation satisfies the following condition:

$$c_{i,im}^{T_m} + c_{im,i}^{T_e} \geqslant 0 \tag{23}$$

for each interior edge connecting nodes i and im.

Most of the today available mesh-generators satisfy the Delaunay property, even if some exceptions may occur around internal boundaries, or when the mesh density is forced to change in given sub-domains. If the Delaunay property is not satisfied (see Fig. 2(b)), it is still possible to obtain a new mesh that satisfies condition (23) for all the internal edges starting from the original one, without changing the location of the original nodes. This can be done by a series of local edge swaps, where two elements sharing the same edge are changed in a new couple, sharing the same nodes but having a different edge, connecting the two nodes opposite to the previous edge. See for example the new triangles obtained in Fig. 3(b) by the original ones of Fig. 3(a). It can be
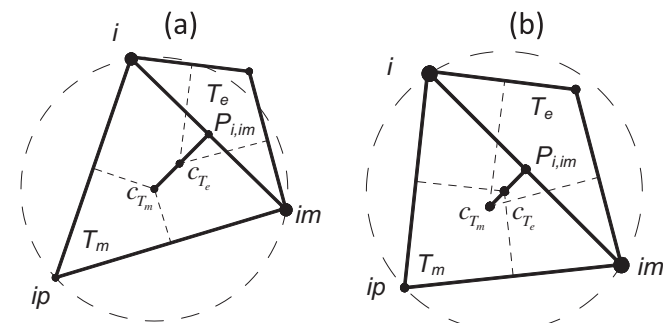

Fig. 2. Delaunay condition: (a) triangles T_m and T_e satisfy Delaunay condition; (b) triangles T_m and T_e do not satisfy Delaunay condition.

shown [17] that the common edge satisfies the Delaunay property in at least one of the two configurations. By iterating the same control for all the edges, the Delaunay property is quickly attained for all the edges of the mesh that are shared by two triangles.

Condition (23), if satisfied for all the internal edges, implies the negative sign of the corresponding extra-diagonal coefficients in Eq. (21) only if the medium is homogeneous. Moreover, if element T_m is a boundary element and $\mathbf{r}_{i,im}$ is a boundary edge opposite to an obtuse angle the flux coefficient, proportional to $c_{i,im}^{T_m}$, remains negative, even if the mesh satisfies the Delaunay property, because the distance of the circumcenter from the boundary edge is negative.

We define Generalized Delaunay (GD) mesh a Delaunay mesh where condition (23) holds for all the internal edges and

$$c_{i,im}^{T_m} \geqslant 0 \tag{24}$$

holds for all the boundary edges. If condition (24) does not hold for one or more boundary edges, and/or common edges are fixed as internal boundaries, it is still possible to obtain a GD mesh, also saving the internal boundaries, by simply adding a small number of nodes along the boundary sides. See in [2] the required procedure.

According to the definition of coefficient $\chi_{j,jp}^{m,e}$ given in Eq. (21), in the case of Delaunay triangulation and homogeneous medium the matrix of the linear system is positive definite and satisfies the M-property. As mentioned in the introduction, in heterogeneous media these 'nice' properties of the linear system depend on the distribution of the permeability K inside the domain.

Given a GD mesh, we propose to change the formulation of coefficient $\chi_{j,jp}^{m,e}$ given in (21), in order to always preserve the M-matrix property and the positive definite condition even in the case of heterogeneous medium, by setting:

$$\chi_{j,jp}^{m,e} = \min\left(big, \frac{|\mathbf{r}_{j,jp}|}{\left(\frac{c_m}{K_m} + \frac{c_e}{K_e}\right)}\right), \tag{25}$$

where coefficients c_e and c_m are defined as:

$$\begin{aligned}
c_m &= c_{j,jp}^{T_m} \quad c_e = c_{jp,j}^{T_e} \quad \text{if} \quad c_{j,jp}^{T_m} > 0, \quad c_{jp,j}^{T_e} > 0, \\
c_m &= c_{j,jp}^{T_m} + c_{jp,j}^{T_e} \quad c_e = 0 \quad \text{if} \quad c_{j,jp}^{T_m} > 0, \quad c_{jp,j}^{T_e} \leqslant 0 \quad \text{and} \quad |c_{jp,j}^{T_e}| < c_{j,jp}^{T_m}, \\
c_m &= 0 \quad c_e = c_{j,jp}^{T_m} + c_{jp,j}^{T_e} \quad \text{if} \quad c_{jp,j}^{T_e} > 0, \quad c_{j,jp}^{T_m} \leqslant 0 \quad \text{and} \quad |c_{j,jp}^{T_m}| < c_{jp,j}^{T_e}
\end{aligned} \tag{26}$$

and big is a very large positive number (say $big \simeq 1.\text{d}+15$). According to Eqs. (25) and (26), stiffness matrix always satisfies the M-property, is symmetric and positive definite, with the only requirement of constraints (23) and (24). A preconditioned conjugate gradient using the incomplete Cholesky factorization is applied for the solution of system (20) in the unknowns H_m, $m = 1,\ldots,N_T$.

Observe that the flux formulation between the two nodes i and im given in Eq. (19) using coefficient $\chi_{j,jp}^{m,e}$, modified according to Eqs. (25) and (26), is consistent with the Darcy law. If the two triangles sharing nodes i, im are acute triangles, formulations (21) and (25) overlap; if one of the two triangles is obtuse, the flux computed according to formulation (25) is still equal to the flux through the side between nodes i and im, due to a H gradient between the two triangles circumcenters c_{T_m} and c_{T_e}, computed according to the Darcy law and to the permeability of the acute triangle where the segment between c_{T_m} and c_{T_e} is entirely located (see Fig. 2(a)). In this case, the flux computed with the coefficients given by the original Eq. (21) is different and is not consistent with the Darcy velocity occurring in the acute triangle.
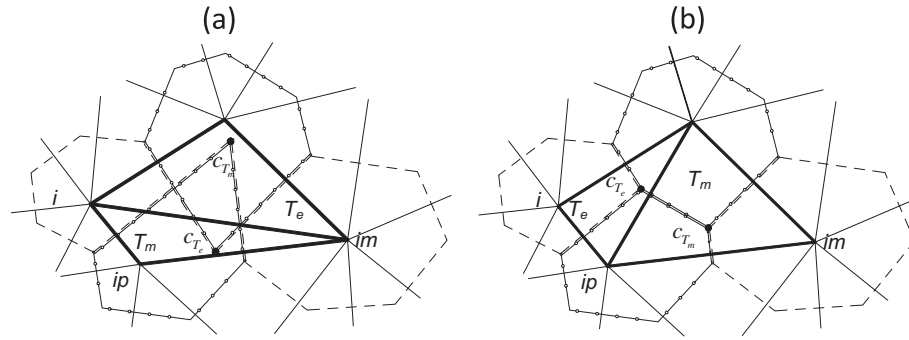
Fig. 3. (a) Original not Delaunay triangulation; (b) Delaunay triangulation after edge swap.

4. Solution of the transport problem

The transport problem in Eq. (3) can be written as:

$$R\varepsilon\frac{\partial C}{\partial t} + L_p + L_c = f_C, \tag{27}$$

where L_p and L_c are differential operators, acting respectively on the convective/reaction and the diffusion terms. The prediction step becomes:

$$R\varepsilon\frac{\partial C}{\partial t} + L_p = f_C \quad \text{with} \quad L_p = \nabla \cdot (\mathbf{q}C) + R\varepsilon\lambda C, \tag{28}$$

while correction step is:

$$R\varepsilon\frac{\partial C}{\partial t} + L_c = 0 \quad \text{with} \quad L_c = -\nabla \cdot (\mathbf{D}\nabla C). \tag{29}$$

4.1. The prediction problem

The MAST scheme is applied for the solution of the convective/reactive transport components. At the beginning of each time step, the computational cells (triangles) are ordered according to their circumcenter potential value and sequentially solved, one after the other, according to the decreasing potential value. It can be easily shown [4,1] that average mass fluxes entering in each cell from neighboring cells with higher potentials are always known before the cell solution. Initial condition at each iteration is given by the solution obtained with the correction step of the previous time iteration. A piece-wise spatial linear approximation $C(\mathbf{x},t)$ of the concentration C inside each cell at any time is assumed (see Fig. 4(a)). Call $C_1^e(t), C_2^e(t)$ and $C_3^e(t)$ the values of C at the three nodes of element T_e, one of the neighboring triangles of T_m with

$H_e > H_m$. Assume a 2nd order polynomial time approximation $\xi_1^e(t), \xi_2^e(t)$ and $\xi_3^e(t)$ of the concentrations at the nodes of the cell T_e, from the beginning (time level t^k) to the end of the time step (time level $t^{k+1/2}$). The time approximation can be written as:

$$\xi^e(t) = \xi^{e,0} + \xi^{e,1}t + \xi^{e,2}t^2, \tag{30}$$

where ξ^e is a vector with components ξ_1^e, ξ_2^e and ξ_3^e. Call j (j = 1, 2, 3) the index of the side of T_e shared with T_m with nodes j and jp (jp is the node following node j in counterclockwise direction). The incoming flux in the downstream (in the potential scale) cell T_m is known at any time as the product of the mean concentration value between ξ_j^e and ξ_{jp}^e times the volumetric flux.

The basic idea of the algorithm is to force the spatial linear approximation of $C(t)$ inside cell T_m to have at time $t + dt$ the same 0th and 1st order spatial moments of the analytical solution obtained at the same time level starting from a linear initial distribution at time t, as shown in Fig. 4(b) (for simplicity a 1D case is shown). 1st order moments are computed with respect to the centroid of the triangular element with co-ordinates $\mathbf{x}_G^m$. Decay term $\lambda R\varepsilon C$ and source term f_C are assumed concentrated in the centroid of each element, so that their 1st order x_1 and x_2 moments are zero. According to this, the following ODEs system is obtained for each triangle T_m in the three nodal concentrations unknowns:

$$\frac{d\mathbf{C}^m}{dt} = \mathbf{A}^m\mathbf{C}^m + \mathbf{b}(t), \tag{31}$$

where $\mathbf{b}(t)$ is a polynomial of the same order of ξ^e,

$$\mathbf{b}(t) = \mathbf{b}^0 + \mathbf{b}^1 t + \mathbf{b}^2 t^2 \quad 0 \leqslant t \leqslant \Delta t \tag{32}$$

and the vectors $\mathbf{b}^0$, $\mathbf{b}^1$ and $\mathbf{b}^2$ are given in Appendix A, as well as matrix $\mathbf{A}^m$ coefficients.
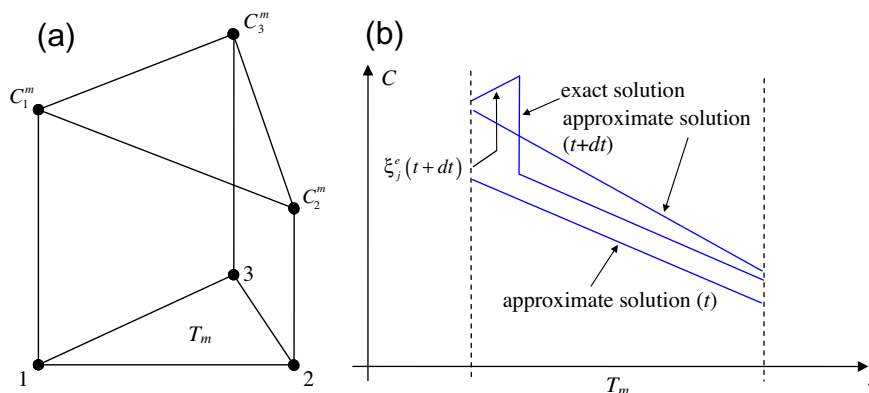

Fig. 4. (a) Spatial concentrations distribution at the three nodes of triangle T_m; (b) equality of the 1st order spatial moment of exact and approximate solutions inside cell T_m.

Because of its asymmetry, matrix $\mathbf{A}^m$ can have either three real or one real and two conjugate eigenvalues and eigenvectors. It is shown, in [4,1], that the solution of system (31) at the end of time step is given by:

$$\mathbf{C}^m = \alpha_1 \mathbf{C}_1^m + \alpha_2 \mathbf{C}_2^m + \alpha_3 \mathbf{C}_3^m + \mathbf{v}^0 + \mathbf{v}^1 \Delta t + \cdots + \mathbf{v}^n \Delta t^n, \qquad (33)$$

where the first three terms are the solution of the homogeneous part of Eq. (31) and coefficients α_1, α_2 and α_3 are computed by forcing the solution of system (31) to honour the initial concentration values at the three nodes of the cell (see Appendix A). $\mathbf{C}_1^m$ and $\mathbf{C}_2^m$ and $\mathbf{C}_3^e$ are functions of the eigenvalues and eigenvectors of $\mathbf{A}^m$ and their expressions are given in Appendix A. Vectors $\mathbf{v}^i$ ($i = 0, 1, 2$) can be computed by comparing terms in the polynomial part of Eq. (31) with the same time exponent (see Appendix A). Once the ODEs system (31) is solved, polynomial coefficients in Eq. (31) have to be computed. Since a 2nd order polynomial has been assumed, coefficients in Eq. (30) can be set in order to honour the computed initial and final values, as well as to match the mean in time value of each polynomial approximation with the one computed from the analytical solution (see Appendix A).

A function limiter has been later on introduced in the algorithm to ensure monotonicity of the solution [1]. Due to the existence of the diffusion terms, monotonicity is usually attained and the above mentioned function limiter has not been activated in the present algorithm.

4.2. The correction problem

Three concentration nodal values for each triangle are computed in the prediction step, so that for each node one obtains a number of concentration values equal to the number of triangles sharing the same node.

Before the correction diffusive step, the continuity of the concentrations along the element sides is restored by computing, in each node, the single concentration that maintains the total mass around the same node. This concentration is equal to:

$$C_i = \frac{\sum_{m=1,N_T} \left(\sum_{j=1,2,3} C_j^m |T_m| \delta_{i,j} \right)}{\sum_{m=1,N_T} \left(\sum_{j=1,2,3} |T_m| \delta_{i,j} \right)} \delta_{i,m} \quad i = 1, \dots, N, \qquad (34)$$

where $\delta_{i,m}$ is equal to 1 or 0 according if node i is a node of triangle T_m or not and $\delta_{i,j}$ is equal to 1 or 0 according if the jth node of T_m is equal to i or not. The dual finite control volume associated with node i is the closed polygon given by the union of the midpoint of each side with the "anisotropic" circumcenter (further defined) of each triangle sharing node i. Storage capacity is assumed to be concentrated in the nodes in the measure of 1/3 of the area of all triangles sharing the same node. After space and fully implicit time integration, mass balance can be written as:

$$\sum_{T=1,N_T} \frac{|T_m| \delta_i^{T_m}}{3} R_i \varepsilon_i \frac{C_i^{k+1} - C_i^{k+1/2}}{\Delta t} + \sum_{T=1,N_T} \left(F_{i,ip}^{T_m} \left(C_{ip}^{k+1} - C_i^{k+1} \right) \right.$$
$$\left. + F_{i,im}^{T_m} \left(C_{im}^{k+1} - C_i^{k+1} \right) \right) \delta_{i,m} = 0, \quad i = 1, \dots, N, \qquad (35)$$

where R_i and ε_i are respectively the values of R and ε in node i. These are computed as a weighted mean of the R and ε values holding in the triangles sharing node i. $\delta_{i,m}$ is above specified, ip and im are the other two nodes of T_m. Apices $k + \frac{1}{2}$ and $k + 1$ mark the beginning and the end of the time step. The second summation on the l.h.s. of system (35) represents the spatial discretization of the diffusive operator $-\nabla \cdot (\mathbf{D}\nabla C)$, $F_{i,ip}^{T_m}$ and $F_{i,im}^{T_m}$ are the flux coefficients, that is the flux from ip to i and from im to i, due to a unitary difference of concentration between nodes ip and i and im and i, computed across the two sides of the control volume of node i lying in triangle T_m (see Fig. 5(b)) The same preconditioned conjugate gradient method used to solve the flow linear system resulting from the time integration of Eq. (20) is used to solve the correction system (35).

4.2.1. The anisotropic circumcenter

Assume a full diffusion tensor $\mathbf{D}$, related to velocities through Eq. (4), to be constant within each triangular element. The tensor elements are obtained by averaging the three nodal values, as explained in [3]. Let T_m be a triangular element of the domain, with nodes i, ip and im, as specified in Section 3. Call $\tilde{c}_{T_m}$ the anisotropic circumcenter of triangular element T_m and $\mathbf{x}_c^{T_m}$ its spatial co-ordinate vector. Call $P_{i,ip}$ and $P_{i,im}$ the midpoints of edges $\mathbf{r}_{i,ip}$ and $\mathbf{r}_{i,im}$, with $\mathbf{x}_{i,ip}$ and $\mathbf{x}_{i,im}$ the corresponding co-ordinate vectors. The anisotropic circumcenter is computed in order to set to zero the flux across segments $|P_{i,ip}\tilde{c}_{T_m}|$ and $|P_{i,im}\tilde{c}_{T_m}|$ due to the component of $\mathbf{D}\nabla C$ orthogonal to edges $\mathbf{r}_{i,ip}$ and $\mathbf{r}_{i,im}$. This is equivalent to set the above mentioned fluxes equal to:

$$Fn_{i,ip}^{T_m} = -\mathbf{D}\mathbf{n}_{i,ip} \wedge \left(\mathbf{x}_c^{T_m} - \mathbf{x}_{i,ip} \right) = 0 \quad \text{and}$$
$$Fn_{i,im}^{T_m} = -\mathbf{D}\mathbf{n}_{i,im} \wedge \left(\mathbf{x}_c^{T_m} - \mathbf{x}_{i,im} \right) = 0, \qquad (36)$$

where $\mathbf{n}_{i,ip}$ and $\mathbf{n}_{i,im}$ are the inward unit vectors orthogonal to the edges $\mathbf{r}_{i,ip}$ and $\mathbf{r}_{i,im}$ respectively (see Fig. 5(a)). Since $\mathbf{D}$ is a full tensor, sides $\mathbf{r}_{i,ip}$ and $\mathbf{r}_{i,im}$ are generally not orthogonal to vectors $-\mathbf{D}\mathbf{n}_{i,ip}$ and $-\mathbf{D}\mathbf{n}_{i,im}$.

An isotropic problem can be regarded as a particular case of the anisotropic one, where full tensor $\mathbf{D}$ becomes a positive scalar value D and sides $\mathbf{r}_{i,ip}$ and $\mathbf{r}_{i,im}$ are orthogonal to vectors linking circumcenter of triangle with their midpoints.

4.2.2. Computation of the diffusion flux coefficients

According to the computation of $\tilde{c}_{T_m}$, fluxes across $|P_{i,ip}\tilde{c}_{T_m}|$ and $|P_{i,im}\tilde{c}_{T_m}|$ are due only to the component of $\mathbf{D}\nabla C$ along the $\mathbf{r}_{i,ip}$ and $\mathbf{r}_{i,im}$ directions and do not depend on the C values of the opposite nodes (respectively im and ip). The structure of the flux across the segment from the edge midpoint to the triangle anisotropic
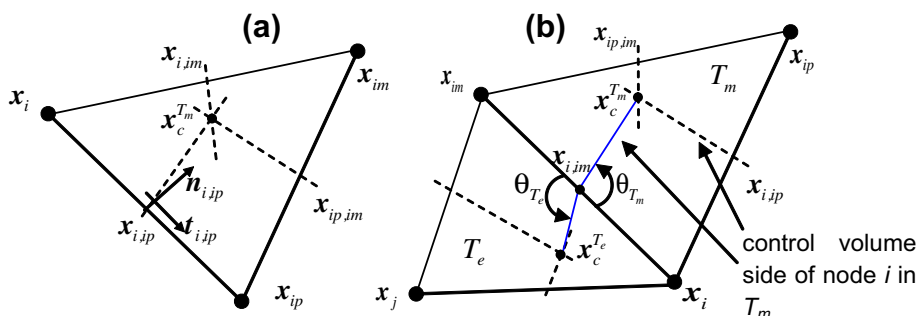

Fig. 5. (a) Element notation; (b) computation of matrix coefficient $Fd_{i,im}$.

circumcenter is similar to the one of the $P1$ Galerkin scheme (see for example [32]). Flux coefficients across $|P_{i,ip}\tilde{c}_{T_m}|$ and $|P_{i,im}\tilde{c}_{T_m}|$ due to a unitary differences of C values in nodes ip and i, as well as in im and i, are computed as (see [3], Appendix B and Fig. 5(a)):

$$F_{i,ip}^{T_m} = -\mathbf{D}(\mathbf{x}_{ip} - \mathbf{x}_i) \wedge (\mathbf{x}_c^{T_m} - \mathbf{x}_{i,ip}) \frac{1}{|\mathbf{r}_{i,ip}|^2} \quad \text{and} \quad F_{i,im}^{T_m}$$

$$= -\mathbf{D}(\mathbf{x}_i - \mathbf{x}_{im}) \wedge (\mathbf{x}_c^{T_m} - \mathbf{x}_{i,im}) \frac{1}{|\mathbf{r}_{i,im}|^2}. \tag{37}$$

$\tilde{c}_{T_e}$ is the anisotropic circumcenter of T_e, sharing side $\mathbf{r}_{i,im}$ with element T_m (see Fig. 5(b)). In the stiffness matrix of the resolving system (35), the global extra-diagonal coefficient $F_{i,im}$ corresponding to the connected nodes i ad im is given by the sum of the flux coefficients in T_m and T_e across $|P_{i,ip}\tilde{c}_{T_m}|$ and $|P_{i,im}\tilde{c}_{T_m}|$ (see Fig. 5(b)), that is:

$$F_{i,im} = F_{i,im}^{T_m} + F_{im,i}^{T_e}, \tag{38}$$

with $F_{i,im}^{T_m}$ and $F_{im,i}^{T_e}$ given in Eqs. (37). Eq. (38) can be written as (see [3] and Appendix B):

$$F_{i,im} = -\frac{\left(d_{i,im}^{T_m} \tilde{c}_{i,im}^{T_m} \sin\theta_{T_m} + d_{im,i}^{T_e} \tilde{c}_{im,i}^{T_e} \sin\theta_{T_e}\right)}{|\mathbf{r}_{i,im}|^2}, \tag{39}$$

with

$$d_{p,pm}^{T_q} = |\mathbf{D}^{T_q}(\mathbf{x}_p - \mathbf{x}_{pm})|, \quad q = \begin{Bmatrix} m \\ e \end{Bmatrix}, \quad p = \begin{Bmatrix} i \\ im \end{Bmatrix}, \quad pm = \begin{Bmatrix} im \\ i \end{Bmatrix} \tag{40}$$

and $\tilde{c}_{p,pm}^{T_q}$ is the distance between $\tilde{c}_{T_q}$ and midpoint $P_{i,im}$ in triangle T_q, computed similarly to Eq. (18), θ_{T_q} is the angle between vectors $\mathbf{D}^{T_q}(\mathbf{x}_p - \mathbf{x}_{pm})$ and $(\mathbf{x}_c^{T_q} - \mathbf{x}_{i,im})$ in T_q. Vectors $(\mathbf{x}_c^{T_1} - \mathbf{x}_{i,im})$ and $(\mathbf{x}_c^{T_2} - \mathbf{x}_{i,im})$ in Fig. 5(b) have different directions since generally $\mathbf{D}^{T_m} \neq \mathbf{D}^{T_e}$.

Observe that extra-diagonal coefficients $F_{i,im}$ have to be always negative in order to guarantee the M-property and the positive definite condition of the system matrix. To guarantee the negative value, at least in the homogeneous case, we change Eq. (39) in the following form:

$$F_{i,im} = -\frac{\left(d_{i,im}^{T_m} \tilde{c}_1 \sin\theta_{T_m} + d_{im,i}^{T_e} \tilde{c}_2 \sin\theta_{T_e}\right)}{|\mathbf{r}_{i,im}|^2}, \tag{41}$$

with $\tilde{c}_q$ ($q = 1, 2$) defined as:

$$\tilde{c}_1 = \tilde{c}_{i,im}^{T_m}, \quad \tilde{c}_2 = \tilde{c}_{im,i}^{T_e} \quad \text{if} \quad \tilde{c}_{i,im}^{T_m} \geqslant 0 \quad \text{and} \quad \tilde{c}_{im,i}^{T_e} \geqslant 0, \tag{42,a}$$

$$\tilde{c}_1 = \tilde{c}_{i,im}^{T_m} + \tilde{c}_{im,i}^{T_e}, \quad \tilde{c}_2 = 0 \quad \text{if} \quad \tilde{c}_{im,i}^{T_e} < 0 \quad \text{and} \quad \tilde{c}_{i,im}^{T_m} \geqslant |\tilde{c}_{im,i}^{T_e}|, \tag{42,b}$$

$$\tilde{c}_1 = 0, \quad \tilde{c}_2 = \tilde{c}_{i,im}^{T_k} + \tilde{c}_{im,i}^{T_e} \quad \text{if} \quad \tilde{c}_{i,im}^{T_m} < 0 \quad \text{and} \quad \tilde{c}_{im,i}^{T_e} \geqslant |\tilde{c}_{i,im}^{T_m}|, \tag{42,c}$$

According to Eqs. (42,a)–(42,c), $\tilde{c}_q$ is never smaller than zero.

In [3] we also show that: (1) it is always possible to split the diffusion tensor defined in each node in a directional times a scalar components, (2) If the directional component of the diffusion tensor is constant inside the domain, it is always possible to apply a swap-based technique to get a final triangulation that leaves unchanged the node location, but guarantees negative extra-diagonal coefficients, (3) in the most general anisotropic heterogeneous case, it is always possible to maintain the M-property and the positive definite condition of the system by applying a parameter smoothing to the two elements sharing an edge corresponding to positive extra-diagonal coefficient, when swapping the edge does not lead to a negative extra-diagonal coefficient.

The previous procedure has been proposed in [3] with constant in time diffusion tensor coefficients. According to Eq. (4), in a time dependent flow field, diffusion coefficients change in time. This makes the diffusive transport problem solution more challenging and poses questions about the stability and robustness of the algorithm proposed for the computation of the diffusive transport problem and the coupling of the two node-based procedures of the numerical solver of the transport problem.

5. Input data structure

The following input data have to be assigned for the solution of the flow and transport problems: (1) the external boundary, defined as a set of edges connecting an equal number of nodes, (2) the internal boundaries, defined by a set of edges, each one associated to a couple of nodes, (3) a set of internal nodes, (4) an initial triangulation of all the nodes.

If the available triangulation does not satisfy the GD condition for one or more internal edges, the iterative edge swaps procedure depicted in Section 3 can be applied. If the GD condition cannot be attained for one or more boundary sides, a small number of nodes can added along these (boundary) sides, as described in Section 3 and in [2].

Once the GD condition for the triangulation is obtained, the following data are also required: (5) the initial conditions, respectively in the elements and nodes, for H and C, (6) the boundary conditions for H and C, (7) a set of physical parameters (s_0, K, ε, R, λ, T_l) for each element of the original GD mesh, to be used for the solution of the flow problem and for the solution of the convective prediction problem, (8) a set of physical parameters for each node of the mesh (D_m, α_L, α_T), to be used for the solution of the diffusion correction problem; the procedure applied for the estimation of the element tensors, in the mesh updated after each change of the velocity field, can be found in [3].

To avoid the need of totally regenerating the dual mesh for the solution of the diffusive transport step starting from the basic GD one after any change of the velocity field, the dual mesh computed for the running time step is saved and used as initial one for the first time step with a new velocity field.

6. Numerical tests

We present six numerical tests. The first one is about the steady state flow field computed in a domain with strong permeability changes, discretized with an unstructured GD mesh with obtuse triangles. A comparison between the performances of the proposed methodology and the standard MHFE formulation [35] is carried out. The second and third tests are aimed to investigate the coupling of the two node-based techniques for transport problem, solved using the same nodes but two different meshes, with assigned flow field and using an analytical solution as reference solution. In tests 4 and 6, the computed results are compared with those obtained by other literature models. In test 4 we deal with a transport problem with assigned flow field, while in test 6 we solve a convection/diffusion and reaction transport problem. The fifth test accounts of a real-like situation with heterogeneous domain, space-dependent permeability coefficients and time-dependent flow field. Robustness of the solution, with particular attention to the diffusive component (affected by the time variation of the diffusion tensor coefficients), is analyzed by refining the computational mesh.

6.1. Test 1. Flow field computation for a steady state problem in a domain with strong permeability changes

The problem is solved over a square domain $[-0.5, 0.5]^2$, discretized using the strongly unstructured GD mesh shown in

Fig. 6 (128 triangles and 81 nodes). Permeability K changes in space according to the following expression, function of the centroids coordinates of each triangle T_m:

$$\widehat{K}_m = e^{\frac{\left(\sin\left(\frac{\pi x_{1,G}^m}{2dx_1}\right) + \sin\left(\frac{\pi x_{2,G}^m}{2dx_1}\right)\right)}{0.01}}, \tag{43}$$

where $dx_1 = 1/8$. The iso-K contours are shown in Fig. 7(a). An analytical solution of the piezometric heads is imposed:

$$H_{ex} = 2 - 4x_1^2(2 - x_1)\exp^{x_1(2-x_1)}x_2(1 - x_2)\exp^{x_2} \tag{44}$$

and the contours of the iso-H are shown in Fig. 7(b). The source term f_H on the r.h.s. of the governing PDEs (1) and (2) is computed by space differentiation of the same solution on the l.h.s. of the same Eqs. (1) and (2) according to the imposed solution in Eq. (44). Full Dirichlet conditions are imposed on the domain boundaries:

$$\Gamma_D^H = \Gamma(\Gamma_N^H = \emptyset) \quad H_D(\mathbf{x}) = H_{ex} \quad \forall \mathbf{x} \in \Gamma. \tag{45}$$

Starting from the mesh in Fig. 6 (coarse mesh), three refinements have been carried out, dividing each triangle in four equal ones by connecting the midpoints of the three sides. After each refinement, a check is carried out in order to verify that the refined mesh satisfies the GD property. If this is not the case, the GD condition is attained by performing a series of edge swaps, as mentioned in Section 3. The new mesh is the starting mesh for the next refinement level. The L_2 norm of the relative error corresponding to the lth refinement level has been computed as:
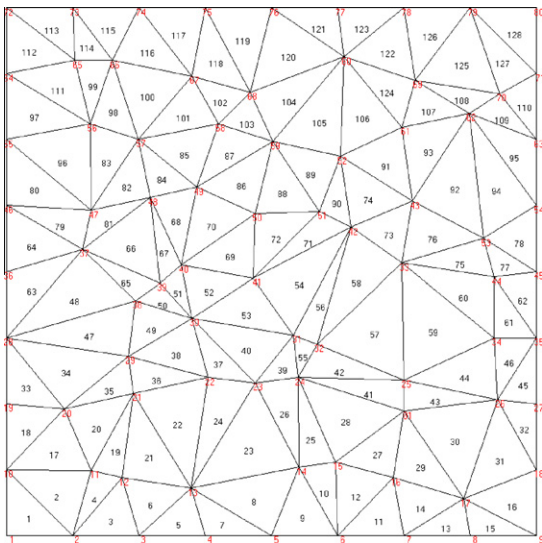
$$err_l = \frac{\sqrt{\sum_{m=1,N_T}(H_m - H_{ex,m})^2}}{\sqrt{\sum_{m=1,N_T}(H_{ex,m})^2}}, \tag{46}$$

where H_m and $H_{ex,m}$ are the computed and the exact solutions at circumcenter of element T_m. The relative error for mesh level l is approximated by a power of the linear size of the area of the mean triangle in the mesh:

$$err_l = \left(\sqrt{|T|_l}\right)^{r_c}, \tag{47}$$

where $|T|_l$ is the area of the mean triangle in the mesh refinement level l and $\sqrt{|T|_l}$ represents a measure of its linear size. The rate of convergence r_c is computed by comparing the relative errors of two consecutive refinement levels l and $l + 1$:

$$r_c = \frac{\log\left(\frac{err_l}{err_{l+1}}\right)}{\log(2)}. \tag{48}$$

In Table 1, the number of elements and the L_2 norm of the relative error for each lth refinement level are reported. Results of the proposed flow field solver are compared with the ones of the standard MHFE scheme [35]. Observe that the relative errors of the MHFE are more than twice the errors of the proposed scheme. This is due to the presence of several obtuse triangles and to the heterogeneity of the permeability in the domain. The convergence order is approximately 2 for both models. Moreover, the matrix of the standard MHFE scheme has order equal to the number of edges, the matrix resulting from the proposed algorithm has order equal to the elements number (that usually is much smaller).

6.2. Analysis of the convergence order of the transport problem solver

6.2.1. Test 2. Smooth assigned solution in a 2D problem

A unitary square domain $\Omega = [0,1]^2$ is assumed with the following assigned flow field: $q_{x_1} = q_{x_2} = 1$ m/s. Decay process is negligible, $R\varepsilon = 1$, $\alpha_L = 100$ m and $\alpha_T = 1$ m. The following analytical solution is assigned:

$$C_{ex} = sin(\pi(x_1 - t))sin(\pi(x_2 - t)) \tag{49}$$

along with full Dirichlet boundary conditions:

$$\Gamma_D^C = \Gamma(\Gamma_N^C = \emptyset) \quad C_D(\mathbf{x}, t) = C_{ex} \quad \forall \mathbf{x} \in \Gamma, \quad \forall t \in [0, T], \tag{50}$$
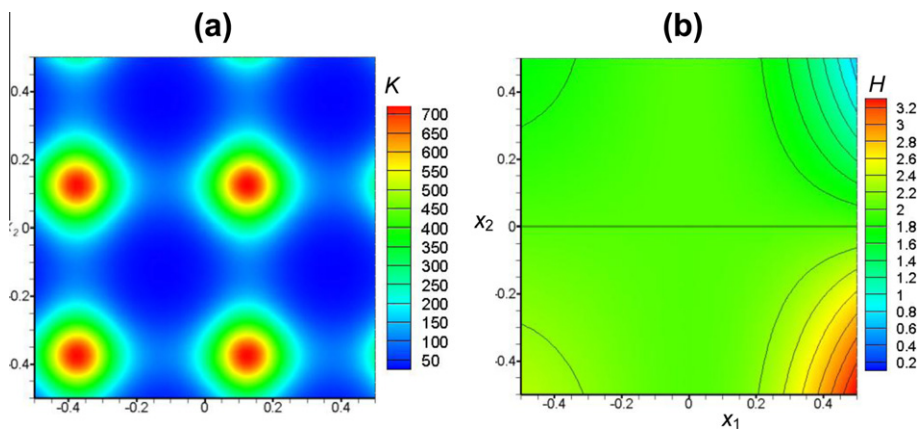

Fig. 6. Test 1. The coarse GD mesh.

Fig. 7. Test 1. (a) contours of the iso-K; (b) contours of the iso-H.

Table 1
Test 1. L_2 norm of relative errors and convergence order of the proposed flow field solver and the MHFE [35].

Refinement level l	N_T	N	L_2 proposed solver	r_c proposed solver	L_2 MHFE	r_c MHFE
0	128	81	1.46d − 02		3.2d − 02	
1	512	289	2.24d − 03	2.7d + 00	6.1d − 03	2.39d + 00
2	2048	1089	4.8d − 04	2.22d + 00	1.5d − 03	2.02d + 00
3	8192	4225	9.1d − 05	2.4d + 00	3.6d − 04	2.06d + 00
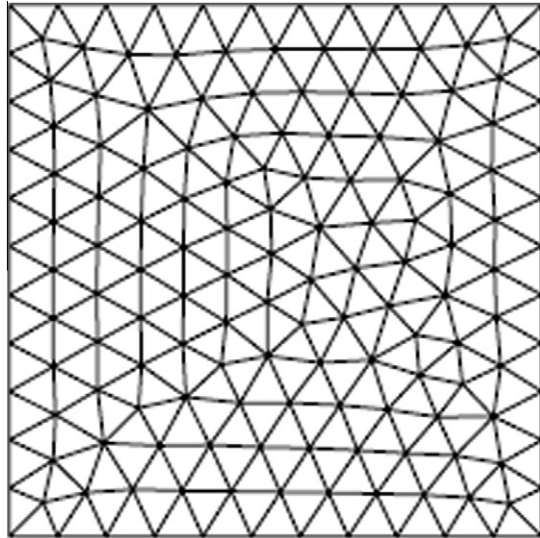
Fig. 8. Test 2. The coarse computational mesh (272 triangles and 159 nodes).

Similarly to the previous test 1, the source term f_C on the r.h.s. of the governing PDEs (27) is computed by space and time differentiation of the same known solution on the l.h.s. of the same Eq. (27). The square domain has been discretized with the unstructured mesh shown in Fig. 8 (coarse mesh, 272 triangles and 159 nodes). Time step size Δt is 0.08 s. The CFL value is computed as:

$$CFL = |\mathbf{q}| \frac{\Delta t}{\sqrt{|T|}} \tag{51}$$

and its maximum value is 2.27. Simulation time is 7.2 s. Starting from the coarse mesh, four refinements have been carried out, as before described. At each mesh refinement, time step has been halved in order to limit the growth of the maximum CFL number.

In Table 2, the number of triangles and nodes of the meshes, as well as the L_2 norms of the relative errors and the convergence order are reported. Analogously the previous test 1, L_2 norm of the relative error corresponding to the lth refinement level is evaluated as:

$$err_l = \frac{\sqrt{\sum_{i=1,N}(C_i - C_{ex,i})^2}}{\sqrt{\sum_{i=1,N}(C_{ex,i})^2}}, \tag{52}$$

where C_i and $C_{ex,i}$ are respectively the computed and the exact solutions at node i.

According to the results computed in Table 2, convergence order increases with mesh refinement, from values smaller than 1 to values close to 1.72. The growth of the convergence order along with the mesh density is very important, because it corresponds to the computation of stable results also when a coarse mesh is used instead of a very refined one.

6.2.2. Test 3. Sharp assigned solution in a nearly 1D problem

An infinite 1D domain $[-\infty, +\infty]$ with assigned flow field ($q_{x_1} > 0$, $q_{x_2} = 0$) is assumed. Decay process is negligible, $R\varepsilon = 1$ and $D_d = 0$. One and zero Dirichlet conditions on the left and right boundary sides have been respectively imposed, as well as initial conditions:

$$C(\mathbf{x}, 0) = 1 \quad x_1 < 0 \quad C(\mathbf{x}, 0) = 0 \quad x_1 \geqslant 0, \quad \forall x_2. \tag{53}$$

The exact solution to this problem is [6]:

$$C(x, t) = 1 - \frac{1}{2} erfc\left(\frac{-(x_1 + v_1 t)}{2\sqrt{\alpha_L |\mathbf{q}| t}}\right), \tag{54}$$

which is not affected by the transverse dispersion coefficient α_T [6]. The transport problem is solved in the 2D domain $[-50, 50] \times [0, a]$ and the numerical solution is not affected by the a value that defines the computational domain. To enhance the 1D character of the test, zero Neumann fluxes along the $x_2 = 0$ and $x_2 = a$ sides are assigned. Value of a is equal to 40 m. Domain has been discretized using an unstructured mesh with 3948 triangles and 2063 nodes (mesh level 0). Time step size is 0.1 s and the total simulation time is 5 s. $q_{x_1} = 1$ m/s, $\alpha_L = 100$ m and $\alpha_T = 1$ m, with a maximum CFL value 1.5. Starting from the computational mesh level 0, three refinements have been performed as previously described. In Table 3, the number of triangles and nodes of the meshes, as well as the L_2 norms of the relative errors and the convergence order are shown. Observe that, eventhough convergence order increases along with the mesh refinement, it is a bit smaller than the one of the previous test. This could be due to the sharper variability of the solution with respect to the one in test 2.

6.3. Test 4. 2D transport problem with known uniform flow field and homogeneous domain

Assume a unitary square domain $\Omega = [0,1]^2$, with full Dirichlet boundary conditions for C:

$$C_D(\mathbf{x}, t) = 1 \quad \forall \mathbf{x} \in \Gamma_{D1}^C \quad C_D(\mathbf{x}, t) = 0 \quad \forall \mathbf{x} \in \Gamma_{D2}^C, \tag{55}$$

with $\Gamma_{D1}^C = [(x_1, x_2): x_1 = 0, 0 \leqslant x_2 \leqslant 1] \cup [0 \leqslant x_1 \leqslant 0.3, x_2 = 0]$ and $\Gamma_{D2}^C = \Gamma - \Gamma_{D1}^C$. $C = 0$ is initially imposed in the domain. The flow field is constant in space and time and the medium is homogeneous.

Table 2
Test 2. L_2 norm of relative errors and convergence order.

Refinement level l	N_T	N	L_2	r_c
0	272	159	5.5d − 01	
1	1088	589	3.2d − 01	7.81d − 01
2	4352	2265	1.4d − 01	1.19d + 00
3	17408	8881	5.1d − 02	1.46d + 00
4	69632	35169	1.55d − 02	1.72d + 00

Table 3
Test 3. L_2 norm of relative errors and convergence order.

Refinement level l	N_T	N	L_2	r_c
0	3948	2063	8.d − 03	
1	15792	8073	4.7d − 03	7.67d − 01
2	63168	31937	2.15d − 03	1.13d + 00
3	252672	127041	8.25d − 04	1.38d + 00

Flow field components are $q_{x_1} = 1$ m/s, $q_{x_2} = 0$ m/s and the following coefficients of the diffusion tensor are assumed: $D_d = 0$ m²/s, $\alpha_L = 1.0d - 01$ m, $\alpha_T = 1.0d - 01$ m (isotropic case), $\alpha_T = 1.0d - 02$ (weak anisotropy) and $\alpha_T = 1.0d - 04$ m (strong anisotropy). Decay process is negligible and $R\varepsilon = 1$. This test has been proposed in [30]. Domain has been discretized using a mesh with 17408 triangles and 8881 nodes, obtained by refining 3 times the one in Fig. 8. $\Delta t = 0.025$ s and the maximum CFL is 2.13.

In Fig. 9, C-isolines computed by the proposed procedure are shown in the case of isotropic medium ($\alpha_L = \alpha_T = 1.0d - 01$ m). C-isolines are undistinguishable from the ones computed in [30] that for brevity are not shown here. The Authors in [30] use a FV Godunov scheme for the solution of convective component, coupled – for the solution of diffusive component – with: 1) a MHFE based on the lowest order Raviart–Thomas (RT_0) approximation of the vector variable (GMM) and 2) a standard $P1$ Galerkin scheme (G-$P1$ M). A limiter is included in the FV Godunov scheme. The Authors in [30] discretize the domain using a mesh with 32768 right-angle triangles and 16641 nodes and use a time step equal to $1.0d - 04$ s for the advective component and $1.0d - 03$ s for the diffusive one, corresponding to a maximum CFL equal to 0.28.

In Fig. 10, the C-isolines computed by the proposed procedure in the weak anisotropic case ($\alpha_L = 1.0d - 01$ m, $\alpha_T = 1.0d - 02$ m) are shown for the simulation times 0.1 s and 0.5 s. Fig. 11 shows the corresponding results computed in [30] using the G-P1 M (dashed lines) and the GMM (solid lines). Also in this weak anisotropic case, results of the three numerical procedures are quite similar.

Reducing the α_T parameter value leads to a reduction of the advancing speed in the central portion of the front (especially at T 0.1 s) and this creates S-shaped C-isolines and steeper front along the x_1 direction in the computed results of the three models. C-isolines computed by the proposed model in the stronger anisotropic case ($\alpha_L = 1.0d - 01$ m, $\alpha_T = 1.0d - 04$ m) are shown in Fig. 12 for the same simulation times. The corresponding results computed by the G-$P1$ M model in [30] are shown in Fig. 13. The G-$P1$ M scheme is stable for this strong anisotropic case while the authors in [30] have observed an ill-conditioning of the GMM scheme. Running the same test without the limiter of the Godunov FV scheme, the Authors in [30] have observed that the G-$P1$ M results do not display any significant difference with the ones obtained using the limiter. On the opposite, the GMM C-isolines reveal unphysical oscillations, especially at 0.1 s, with a maximum C value 1.124.

Results of the proposed model show a front sharper than the one obtained by the G-$P1$ M scheme in [30], but they are free of spurious oscillations. Moreover, in Section 4.1 it has been pointed
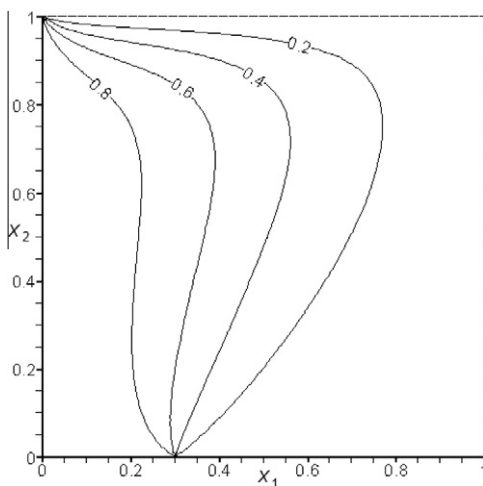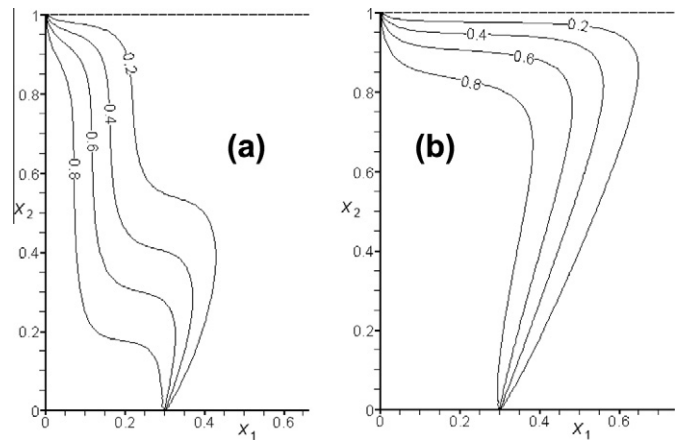

Fig. 10. Test 4. Computed C-isolines ($\alpha_L = 1.d - 01$ m; $\alpha_T = 1.d - 02$ m): (a) $T = 0.1$ s; (b) $T = 0.5$ s.
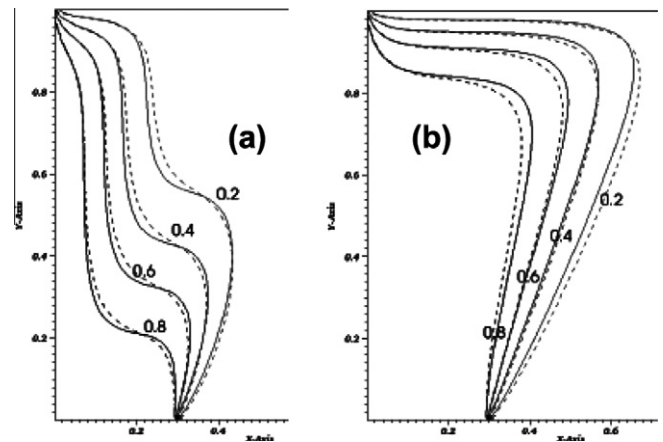

Fig. 11. Test 4. C-isolines computed in [30] (GMM and G-P1 M models) ($\alpha_L = 1.d - 01$ m; $\alpha_T = 1.d - 02$ m): (a) $T = 0.1$ s; (b) $T = 0.5$ s.
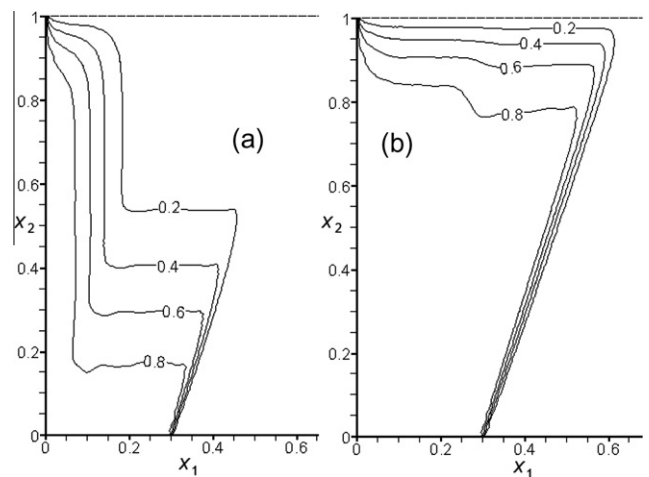

Fig. 12. Test 4. Computed C-isolines ($\alpha_L = 1.d - 01$ m; $\alpha_T = 1.d - 04$ m): (a) $T = 0.1$ s; (b) $T = 0.5$ s.

out that the function limiter of the convective step is not included in the present work. We have refined once more the mesh, but the
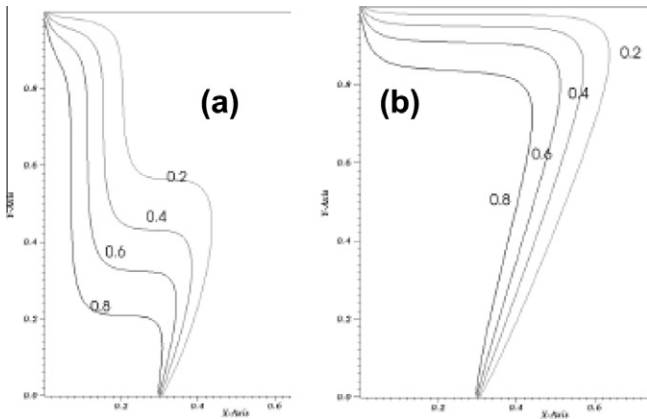

Fig. 9. Test 4. Computed C-isolines ($\alpha_L = \alpha_T = 1.d - 01$ m).

Fig. 13. Test 4. C-isolines computed in [30] (G-P1 M model) ($\alpha_L = 1.d - 01$ m; $\alpha_T = 1.d - 04$ m): (a) $T = 0.1$ s; (b) $T = 0.5$ s.

computed results are practically undistinguishable from the ones in Figs. 12.

6.4. Test 5. Investigation of mesh size effects in a space-dependent permeability and heterogeneous domain. CPU times investigation

A square domain $[0,100]^2$ is assumed, with heterogeneous parameters varying according to the coefficients listed in Table 4.

Table 4
Test 5. Material properties.

Zone	ε [–]	R [–]	λ [s^{-1}]	s_0 [m^{-1}]	D_d [m^2/s]	α_L [m]	α_T [m]
1	0.85	1	0	1.d + 00	0	2.d + 00	1.d − 04
2	0.5	1	0	0.12347d + 00	0	1.d + 00	1.d − 03

The permeability coefficient K is function of the centroid co-ordinates of each triangle T_m:

$$\widehat{K}_m = e^{\frac{\left(\sin\left(\frac{\pi x_{1,G}^m}{4dx_1}\right) + \sin\left(\frac{\pi x_{2,G}^m}{4dx_2}\right)\right)}{10}},$$ (56)

where dx_1 and dx_2 are equal to 9.09091. Zone 1 is $[(x_1,x_2)$, with $0 \leqslant x_1 \leqslant 50$ and $0 \leqslant x_2 \leqslant 100]$, zone 2 is the remaining part of the domain. Full Dirichlet boundary condition equal to 1 is assumed for C and $C = 0$ is the initial condition over all the domain. Boundary conditions for H are:

$$H_D(\mathbf{x},t) = 6 \text{ m} \quad \forall \mathbf{x} \in \Gamma_{D1}^H \quad H_D(\mathbf{x},t) = 1 \text{ m} \quad \forall \mathbf{x} \in \Gamma_{D2}^H,$$ (57)

with $\Gamma_{D1}^H = [(x_1,x_2)$ with $(x_2 = 0$ and $0 \leqslant x_1 \leqslant 100)]$ and $\Gamma_{D2}^H = \Gamma - \Gamma_{D1}^H$. $H_0(\mathbf{x},0) = 1$ m is the initial condition over all the domain. Domain has been discretized using an unstructured mesh with 272 triangles and 159 nodes (coarse mesh). Four refinements have been tested. Total simulation time is 7.5d + 06 s, time step size for the coarse mesh is 50000 s and it has been halved at each refinement. Fig. 14(a) shows the contour lines of the permeability coefficient. Fig. 14(b) shows the computed H-isolines for the 2nd refinement level at the end of simulation time (results obtained with the other meshes are qualitatively very close and are not shown for brevity). Fig. 14(c) represents, in each element, the angles between the two couples of eigenvectors of diffusive tensor computed at two consecutive time iterations. The average normalized change of the tensor elements per each time step, due to the velocity change, is about 10%. Fig. 15 shows the C-isolines contours for the coarse mesh and for the three refinement levels. Results show the stability of the diffusive transport solution with respect to both the mesh and the time step changes occurring at each mesh refinement. Computational costs of the different algorithm steps have been investigated. In Table 5, the mean computational times (in s) per iteration, required for computation of the flow field, cell
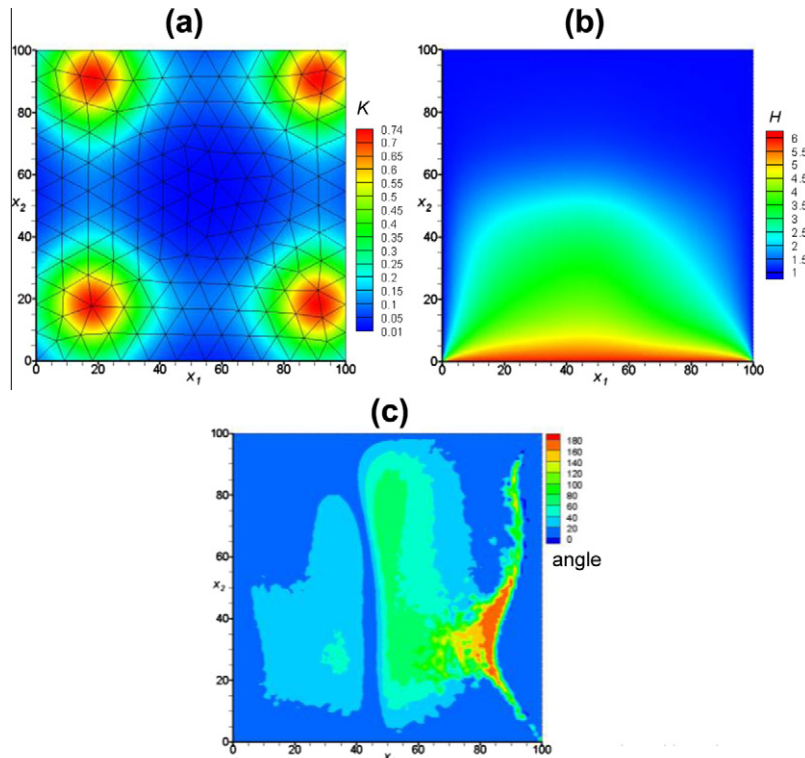

Fig. 14. Test 5. (a) spatial permeability distribution and domain discretization using the coarse mesh; (b) computed H-isolines (2nd refinement mesh level); (c) angles between two couples of eigenvectors of diffusive tensor computed at two consecutive time iterations.
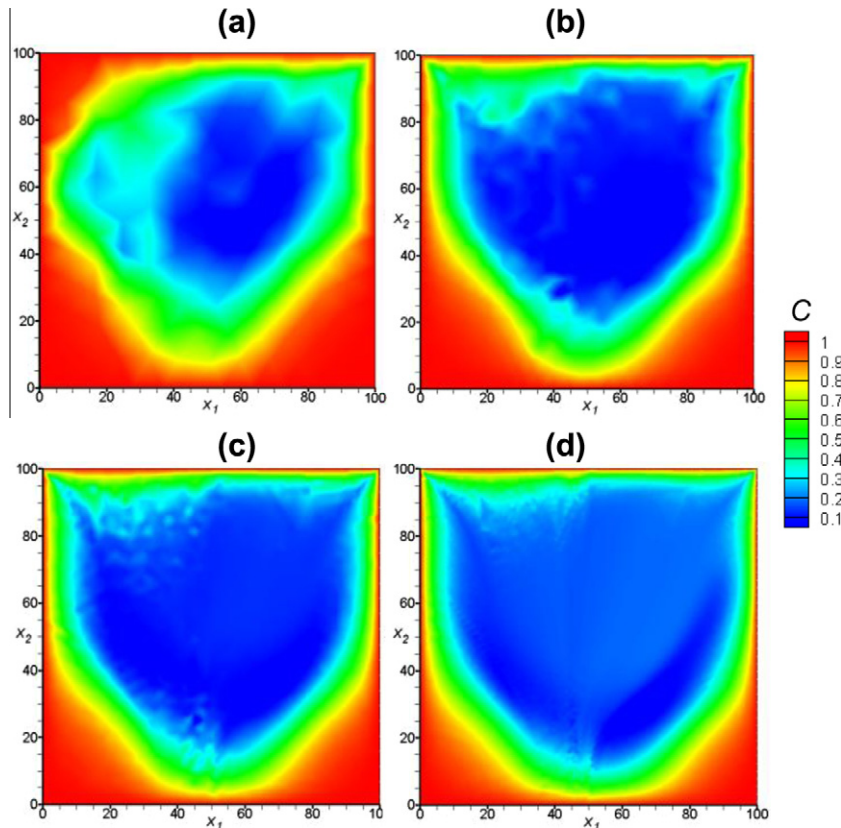
Fig. 15. Test 5. Computed C-isolines ($T = 7.5\mathrm{d} + 06\,\mathrm{s}$). (a) coarse mesh; (b) 1st refinement level; (c) 2nd refinement level; (d) 3rd refinement level.

ordering, solution of the prediction and of the correction steps are reported. In the same table, the mean CPU time per iteration required for the diffusive flux coefficients estimation, that guarantees the M-property of stiffness matrix of the diffusive system, is shown too. The mean CPU times have been computed by dividing the total times required by the different steps by the number of triangles N_T. A single processor Intel Q 6600, 2.40 GHz has been used. The computation of the prediction step of the transport problem is the most demanding one. The mean CPU time for the correction step solution is approximately twice of the CPU time for the flow field solution. Observe that the mean CPU time for the prediction step is almost independent from the mesh elements number, since this represents the "explicit" component of the method. Mean CPU times of the correction step and of the flow field solution increase with the element number. In fact these steps, representing the "non explicit" component of the algorithm, require the solution of large linear systems of the order of the elements and nodes number. The growth is much less than linear. The ordering step requires a CPU time per single cell one-two magnitude orders less than the CPU time required by the correction step. The small reduction of the mean CPU time required for the diffusive flux coefficient estimation in the correction step can be explained with the decreasing ratio between the number of swapped edges and the total number of edges. The growth rate β of the CPU time is measured as the power exponent of the relationship:

$$\overline{CPU} = (N_T)^\beta \Rightarrow \log(\overline{CPU}) = \log(N_T) \cdot \beta + c, \tag{58}$$

where $\overline{CPU}$ is the mean CPU time per iteration and c is an arbitrary constant. In Fig. 16 exponent β ranges from 0.2407 to 0.2564 for the CPU times of the "non explicit" components.

6.5. Test 6. The Andra COUPLEX 1 test

This is one of the COUPLEX benchmarks [9], a set of simplified albeit realistic test cases aimed at simulating the transport of radionuclides around a nuclear waste repository. In the present case the transported pollutant is iodine I 129.

The problem raises some difficulties. In this test, in facts, we handle a highly elongated medium (width-to-height ratio is over 30) with four geological layers and highly variable parameters in space (hydraulic conductivities vary over six orders of magnitude and convection and diffusion constants are very different from one layer to another), highly concentrated sources in space and time and very different time scales. Iodine leaks from containers

Table 5
Test 5. Mean CPU times values for the different algorithm steps and refinement levels.

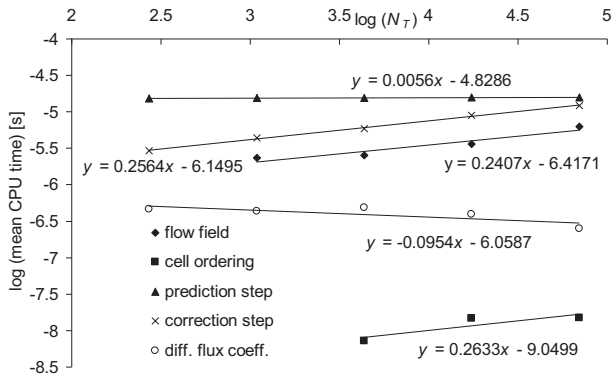| Refinement level	N_T	Flow field	Cell ordering	Prediction step	Correction step	Diff. flux coeff.
0	272	2.13d − 06	0	1.608d − 05	2.68d − 06	3.829d − 07
1	1088	2.489d − 06	0	1.527d − 05	4.787d − 06	4.24d − 07
2	4352	2.848d − 06	1.196d − 08	1.538d − 05	6.88d − 06	5.1d − 07
3	17408	3.6d − 06	1.48d − 08	1.568d − 05	8.96d − 06	3.93d − 07
4	69632	6.29d − 06	1.201d − 08	1.573d − 05	1.217d − 05	3.489d − 07

Fig. 16. Test 5. CPU times of the different step in the proposed procedure. Exponents β.

(repository) into the clay within a short period compared with the millions of years over which convection and diffusion remain active. Geometry of the domain is shown in Fig. 17. Repository $\Re$ is a uniform rectangular source in the clay layer: $\Re =$ (18440 m, 21680 m) $\times$ (244 m, 250 m). Water flows slowly through those porous media and convects the radioactive materials once the containers start to leak. Simulation time is 1.0d + 07 years. Material physical properties, parameters and half life period for I 129 are reported in Table 6. Zero concentration is assumed at the beginning of the simulation in the domain, while the flow problem is assumed to be steady-state. Boundary conditions for H and C are reported in Table 7 and Fig. 18 shows the release of iodine as function of time [9]. An initial unstructured GD mesh with 31234 triangles and 16133 nodes has been used, with triangle sides lying on the internal boundary among layers. The time step size is 200 years.

Fig. 19 shows the computed H-isolines. In the same figure, the red lines show the boundaries of the four geological layers and the repository. According to the computed H profiles, a change of the velocity field direction occurs at the repository. In Fig. 20, a zoom of the velocity field near the repository is shown. The change of the velocity direction causes a distinct shape of the concentration isolines around the repository.
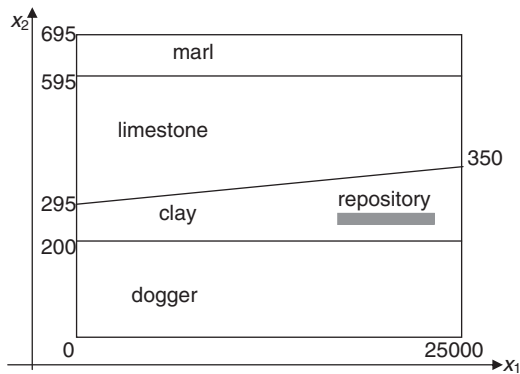
Table 7
Test 6. Boundary conditions for H and C. Values of H in meters, values of C in mol/m^3, distances in meters.

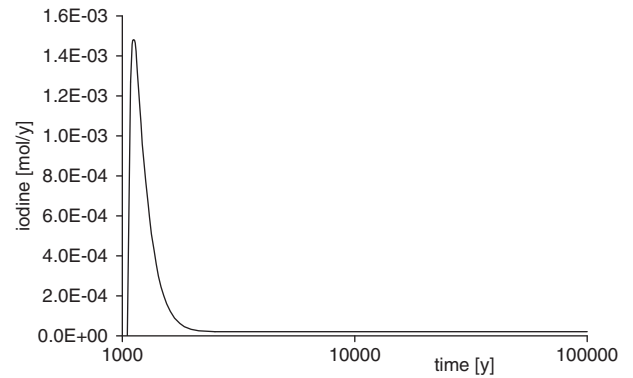| Piezometric head	
$H = 289$	$x_1 = 25000, 0 \leqslant x_2 \leqslant 200$
$H = 310$	$x_1 = 25000, 350 \leqslant x_2 \leqslant 595$
$H = 180 + \frac{160 x_1}{25000}$	$0 \leqslant x_1 \leqslant 25000, x_2 = 695$
$H = 200$	$x_1 = 0, 295 \leqslant x_2 \leqslant 595$
$H = 286$	$x_1 = 0, 0 \leqslant x_2 \leqslant 200$
$\frac{\partial H}{\partial n} = 0$	elsewhere
Concentration	
$\frac{\partial C_i}{\partial n} = 0$	$x_1 = 0, 295 \leqslant x_2 \leqslant 595$
$\frac{\partial C_i}{\partial n} = 0$	$x_1 = 0, 0 \leqslant x_2 \leqslant 200$
$\mathbf{D}_i \nabla C_i \cdot \mathbf{n} - C_i \mathbf{q} \cdot \mathbf{n} = 0$	$0 \leqslant x_1 \leqslant 25000, x_2 = 0$
$C_i = 0$	Elsewhere

Fig. 18. Test 6. Iodine I 129 release in time.

Fig. 17. Test 6. Domain geometry.
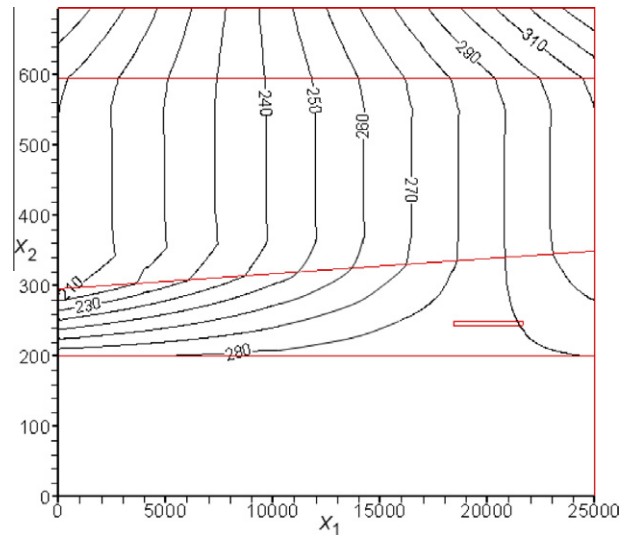
Fig. 19. Test 6. Computed H-isolines.

Table 6
Test 6. Material properties.

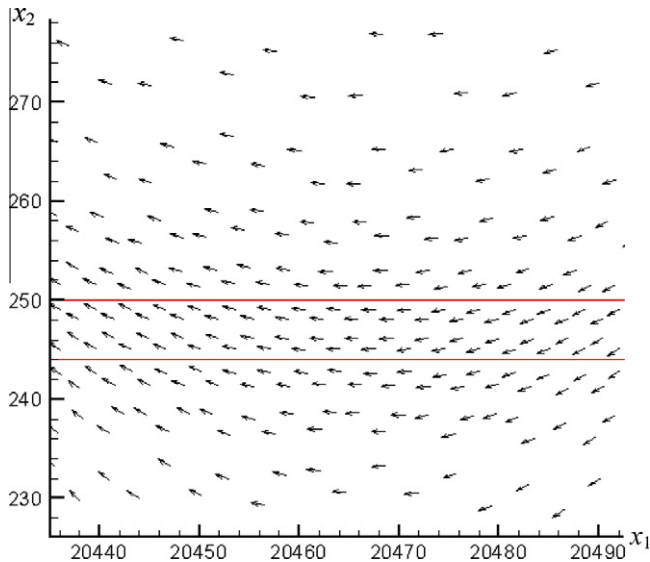| Layer	K [m/year]	D_d [m^2/year]	α_L [m]	α_T [m]	$R\varepsilon$ [-]	T_l I 129 [year]
Marl	$3.1536 \times 1.d-05$	$5.d-04$	0	0	1	$1.57d+07$
Limestone	6.3072	$5.d-04$	50	1	1	$1.57d+07$
Clay	$3.1536 \times 1.d-06$	$5.d-07$	0	0	$1.d-03$	$1.57d+07$
Dogger	25.2288	$5.d-04$	50	1	1	$1.57d+07$

Fig. 20. Test 6. Detail of the flow filed near the repository (in red lines). (For interpretation of the references to colour in this figure legend, the reader is referred to the web version of this article.)
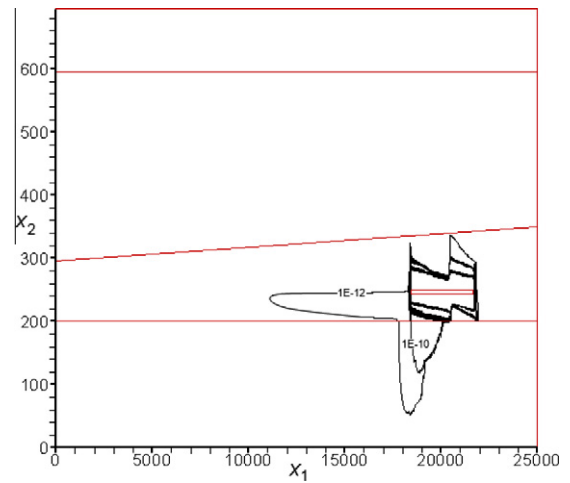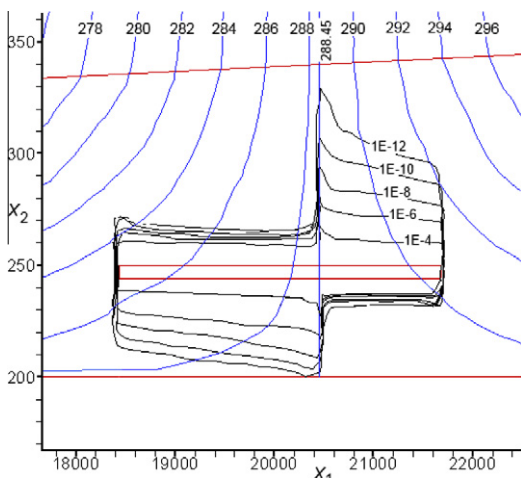

Fig. 21a. Test 6. Detail of the computed C-isolines (black lines) and H-isolines (blue lines) near the repository (red lines) at $T = 10110$ years. (For interpretation of the references to colour in this figure legend, the reader is referred to the web version of this article.)

Fig. 21b. Test 6. Computed C-isolines (black lines) at $T = 10110$ years (in red the boundaries of the geological layers and of the repository).

Fig. 21c. Test 6. Computed C-isolines (black lines) at $T = 50110$ years (in red the boundaries of the geological layers and of the repository). (For interpretation of the references to colour in this figure legend, the reader is referred to the web version of this article.)
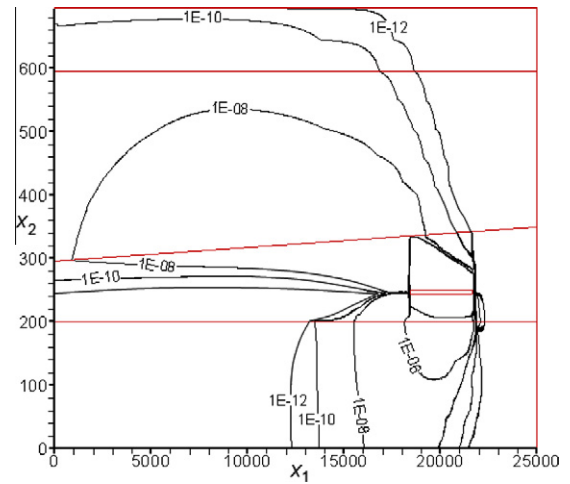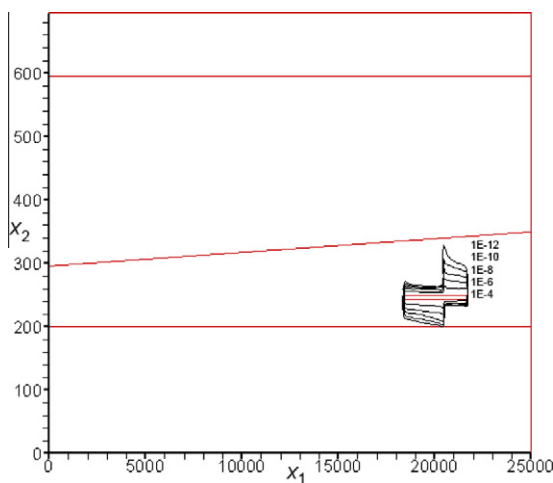

Fig. 21d. Test 6. Computed C-isolines (black lines) at $T = 2.d + 05$ years (in red the boundaries of the geological layers and of the repository). (For interpretation of the references to colour in this figure legend, the reader is referred to the web version of this article.)
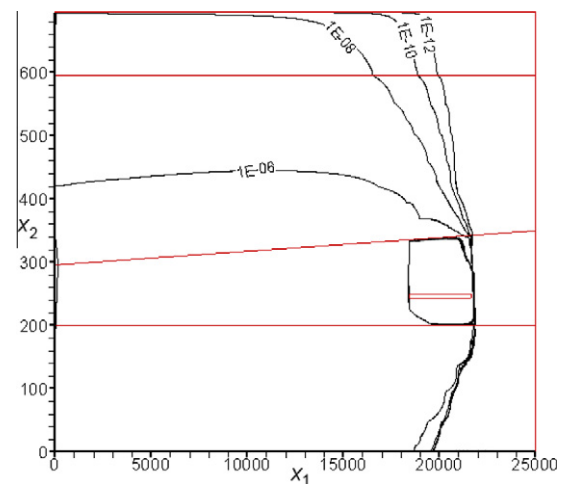

Fig. 21e. Test 6. Computed C-isolines (black lines) at $T = 1.d + 06$ years (in red the boundaries of the geological layers and of the repository). (For interpretation of the references to colour in this figure legend, the reader is referred to the web version of this article.)

Fig. 21f. Test 6. Computed *C*-isolines (black lines) at *T* = 1.d + 07 years (in red the boundaries of the geological layers and of the repository). (For interpretation of the references to colour in this figure legend, the reader is referred to the web version of this article.)
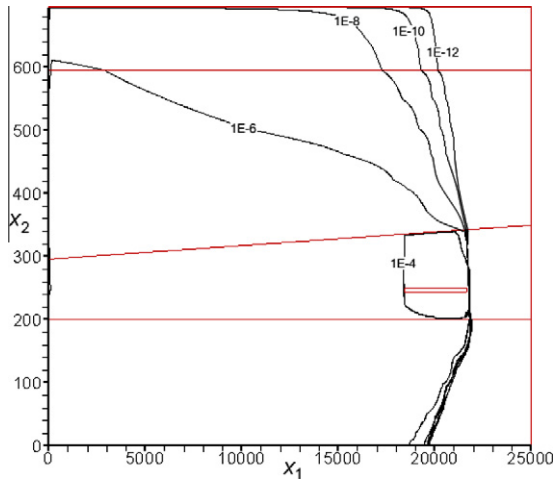
We can look more closely to the portion of $\Re$ on the r.h.s. with respect to the vertical *H*-isoline. In this region the velocity vector, except very close to the vertical *H*-isoline, has a negative vertical component (downward), so that convective and diffusive effects acts along the same direction (downward) in the lower part of the repository, while have opposite direction in the upper portion of repository, where diffusion acts upward and convection downward. Fig. 21a shows a sharp front of concentration in the lower portion of the repository moving downward, while, in the upper
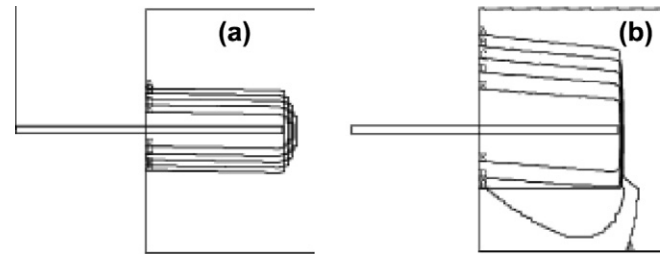

Fig. 22. Test 6. *C*-isolines computed in [8]; (a) *T* = 2.d + 05 years; (b) *T* = 1.d + 06 years; (c) *T* = 1.d + 07 years.

Fig. 23. Test 6. *C*-isolines computed in [8]: (a) *T* = 10110 years; (b) *T* = 50110 years.

region, the diffusion effect spreads out the advected iodine and a smooth concentration profile moves upward. Simulation time is 10110 years.

Exactly the opposite occurs in the region of $\Re$ located on the l.h.s. with respect to the vertical *H*-isoline, where a sharp front moves upward and a smooth profile moves downward.

Observe also that in the two smooth profile regions, the contours of the concentration profiles are affected by the direction of the velocity vectors.

At the beginning of the iodine release, a moderate contaminant mass moves along the x_2 direction, close to the vertical *H*-isoline. This is essentially due to the opposite contaminant mass movements in the right and left domain portions with respect to the vertical *H*-isoline. These small quantities of contaminant mass are then transported by convection and diffusion processes and this explains the higher distances from the repository boundary of the smallest values of the *C*-isolines in the smooth profile regions than in the sharp front regions.

In Figs. 21b–21f, the contours of the *C*-isolines are shown for the simulation times 10110, 50110, 2.0d + 05, 1.0d + 06 and 1.0d + 07 years. Increasing the duration, concentration contours on the r.h.s. and l.h.s. with respect to the vertical *H*-isoline become more uniform around the repository. Computational results have been compared with the ones given by Bernard-Michel et al. [8]. The authors in [8] computed the flow field using a MHFE scheme, and compared the results of three different numerical methods for the solution of the transport problem: a FV, a FE and a MHFE scheme. They discretized the domain using quadrilateral and rectangular grids, with different refinement levels, from 5000 to 166000 elements. More details can be found in [8]. In Fig. 22, results obtained in [8] are shown for the simulation times 2.0d + 05, 1.0d + 06 and 1.0d + 07 years. The pollutant mass inside the domain at the different simulation times, as computed in [8], is less than the one computed by the proposed procedure. At 2.0d + 05 years the *C*-isoline = 1.d-08 mol/m^3 of the proposed model in the limestone layer spreads out for a larger extension than in the FE and MHFE/FV models in [8]. Observe also in the clay layer, on the left side of the repository, a quite different trend of the *C*-isolines 1.0d − 12, 1.0d − 10 and 1.0d − 08 mol/m^3. At 1.0d + 06 years the *C*-isoline 1.0d − 06 mol/m^3 of the proposed model in the limestone layer does not appear in the FE scheme in [8] and the *C*-isoline 1.0d − 04 mol/m^3 computed by the proposed procedure does not cross the repository. At 1.0d + 07 years, the amount of iodine computed in [8] is less than the one computed by the present scheme. It is important to underline that at each simulation iteration, the Mass Balance Ratio (MBR) of the proposed model has been checked out. MBR is defined as [11]:

$$\text{MBR} = \frac{\text{total additional mass in the domain}}{\text{total net flux into the domain}}, \tag{59}$$

where the "total additional mass in the domain" is the difference between the mass measured at any simulation time *t* and the initial
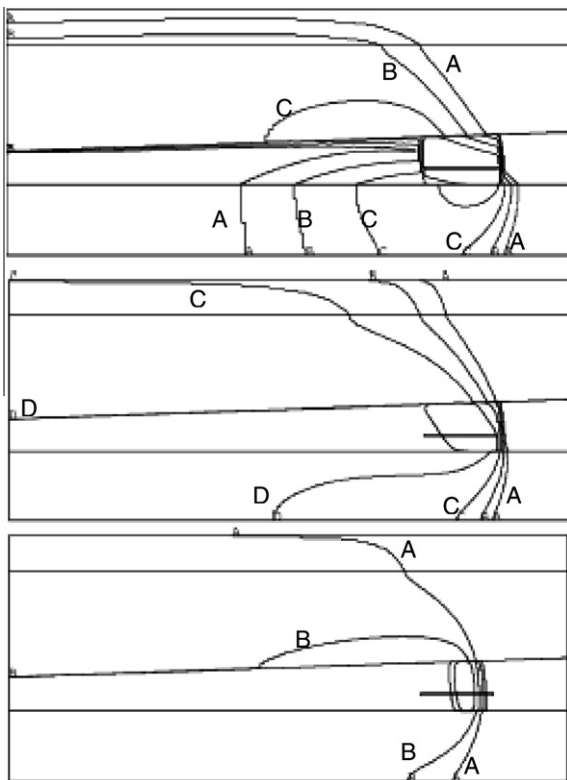
mass in the domain, the "total net flux into the domain" is the flux integrated in time up to time t. In a "perfect" model MBR is equal to 1. For the present simulations the difference (1-MBR) is of the same order of the machine truncation error (1.0d − 15 − 1.0d − 16).

Fig. 23 shows the C-isolines computed in [8] at T = 10110 and 50110 years. These results show a very different trend with respect to the ones computed by the proposed model (in Figs. 21a–21c). In the results by Bernard-Michel et al. [8] the C-isolines around the repository are very smooth and seem to be not affected by the changes in the velocity field on the right and left hand side portions of the domain with respect to the vertical H-isoline, previously discussed.

7. Conclusions

A numerical model for the solution of the flow and transport problem in heterogeneous media with anisotropic diffusion tensor for the transport problem has been presented. The governing PDEs are solved on a given set of nodes, that are connected by an automatically generated triangular mesh. The geometrical input data are the node coordinates, as well as a set of internal and external boundary lines. Flow field is variable in space and time and, in this context, independent from the transport problem. An innovative solution of the flow field guarantees the M-property and the positive definite condition of the matrix of the solution system. Flow field is the basis for the solution of the transport problem, carried out according to a prediction/correction procedure. The prediction step computes analytically the convective/reactive transport components, while the correction step computes the diffusive components.

The proposed flow field solver clearly overruns the original MHFE scheme [35] in the case of heterogeneous medium and unstructured mesh. The coupling of the two node-based techniques of the transport problem is robust, spurious oscillations are missing in the model results and the convergence order of the transport problem solver increases from values less than 1 to values close to 1.72, along with the refining of the mesh. Investigation of mean CPU times per element required by the different model steps reveals that the prediction step of the transport problem is the most demanding one, but it is not affected by the element number. Computation of the flow field, as well as the correction transport step, require a mean cost per element that increases with the element number, but much less than linearly. The swapping procedure in the correction transport step, aimed to guarantee the monotonicity of the solution and the "nice" properties of the linear system, requires a CPU time that is approximately one magnitude order less than the CPU time of the prediction step. The difference between the MBR of an ideal model and the one calculated in the proposed model does not exceed the truncation machine error, that guarantees an almost perfect conservation of mass.

8. Disclosure statement

Appendix A. Solution of the prediction transport problem

In system (31),

$$\frac{d\mathbf{C}^m}{dt} = \mathbf{A}^m\mathbf{C}^m + \mathbf{b}(t) \quad \text{with} \quad \mathbf{C}^m = (\ C_1^m \quad C_2^m \quad C_3^m\ )^T, \tag{A.1}$$

matrix $\mathbf{A}^m$ is given by:

$$A_{ij}^m = \frac{1}{\widehat{\omega}_m} \sum_{q=1,2,3} (B_{iq}^m)^{-1} F_{qj}, \tag{A.2, a}$$

with

$$F_{1j} = -\left(\frac{1-\delta_j}{|T_m|}\int_{l_j^m}\phi_j^m(r_j)dl + \frac{\widehat{\omega}_m\ \widehat{\lambda}_m}{3}\right),$$

$$F_{2j} = -(1-\delta_j)\int_{l_j^m}\phi_j^m(r_j)(x_1 - x_{1,G}^m)dl + \frac{|T_m|q_{x_1}^m}{3}, \tag{A.2, b}$$

$$F_{3j} = -(1-\delta_j)\int_{l_j^m}\phi_j^m(r_j)(x_2 - x_{2,G}^m)dl + \frac{|T_m|q_{x_2}^m}{3}$$

and matrix $\mathbf{B}$ coefficients are:

$$B_{11}^m = B_{12}^m = B_{13}^m = \frac{1}{3},$$

$$B_{21}^m = \frac{|T_m|}{12}\left(2x_{1,1}^m + x_{1,2}^m + x_{1,3}^m\right),$$

$$B_{22}^m = \frac{|T_m|}{12}\left(x_{1,1}^m + 2x_{1,2}^m + x_{1,3}^m\right),$$

$$B_{23}^m = \frac{|T_m|}{12}\left(x_{1,1}^m + x_{1,2}^m + 2x_{1,3}^m\right) \tag{A.3}$$

$$B_{31}^m = \frac{|T_m|}{12}\left(2x_{2,1}^m + x_{2,2}^m + x_{2,3}^m\right),$$

$$B_{32}^m = \frac{|T_m|}{12}\left(x_{2,1}^m + 2x_{2,2}^m + x_{2,3}^m\right),$$

$$B_{33}^m = \frac{|T_m|}{12}\left(x_{2,1}^m + x_{2,2}^m + 2x_{2,3}^m\right),$$

where $\widehat{\omega}_m = \widehat{R_m}\ \widehat{\varepsilon_m}, \widehat{R}_m, \widehat{\varepsilon}_m$ and $\widehat{\lambda}_m$ are the mean spatial values of R, ε and λ in T_m, δ_j is equal to 1 or 0 if the flux is respectively entering or leaving the cell, l_j^m is the length of side j of cell T_m (the side following node j in counterclockwise direction), ϕ_j^m is the flux (positive if leaving the cell) per unit length through the same side of the element, the linear integrals represent the leaving mass and moment fluxes and r_j ($0 \leqslant r_j \leqslant l_j^m$) is the abscissa of the point on side j. Symbol $(.)^T$ in Eq. (A.1) indicates the transpose operator.

Vector $\mathbf{b}(t)$ in Eq. (A.1) is a polynomial of the same order of ξ^e, that is:

$$\mathbf{b}(t) = \mathbf{b}^0 + \mathbf{b}^1 t + \mathbf{b}^2 t^2 \quad 0 \leqslant t \leqslant \Delta t \tag{A.4}$$

and it is equal to:

$$b_i^p = \frac{1}{\widehat{\omega}_m}\sum_{j=1,2,3}(B_{ij}^m)^{-1}G_{jp}, \tag{A.5}$$

where index p marks the order of the polynomial time approximation, p = 0, 1, 2 and

$$G_{1p} = \frac{\delta_j}{|T_e|}\int_{l_{jm}^e}\phi_{jm}^e\xi_{jm}^e(r_{jm})dl + \frac{\widehat{f_{C,p}^m}}{3} \quad G_{2p} = \delta_j\int_{l_{jm}^e}\phi_{jm}^e\xi_{jm}^e(r_{jm})(x_1 - x_{1,G}^m)dl$$

$$G_{3p} = \delta_j\int_{l_{jm}^e}\phi_{jm}^e\xi_{jm}^e(r_{jm})(x_2 - x_{2,G}^m)dl, \tag{A.6}$$

where $\widehat{f_C^m}$ is the mean value of f_C over T_m (generally, a time variation for this term can be assumed known), jm is the side with length l_{jm}^e of any neighboring element T_e (with $H_e > H_m$) shared with

cell T_m (corresponding to side j of T_m), ϕ^e_{jm} is the flux per unit length leaving cell T_e through side jm of the same element and, according to the continuity of fluxes at cell interfaces, $\phi^e_{jm} = -\phi^m_j$; the linear integrals represent the incoming mass and moment fluxes, ξ^e_{jm} is the concentration of the incoming flux of the point on side jm with abscissa r_{jm} ($0 \leqslant r_{jm} \leqslant l^e_{jm}$).

Because of its asymmetry, matrix $\mathbf{A}^m$ can have either three real or one real and two conjugate eigenvalues and eigenvectors. In the first case call λ^m_1, λ^m_2, λ^m_3 and $\mathbf{u}^m_1$, $\mathbf{u}^m_2$, $\mathbf{u}^m_3$ the real eigenvalues and eigenvectors. In the second case call λ^m_3 and $\mathbf{u}^m_3$ the real eigenvalue and eigenvector, λ^m_r, $\mathbf{u}^m_r$ and λ^m_i, $\mathbf{u}^m_i$ the real and the imaginary part of the two conjugate eigenvalues and eigenvectors. The solution of system (31) at the end of time step is given by:

$$\mathbf{C}^m = \alpha_1 \mathbf{C}^m_1 + \alpha_2 \mathbf{C}^m_2 + \alpha_3 \mathbf{C}^m_3 + \mathbf{v}^0 + \mathbf{v}^1 \Delta t + \cdots + \mathbf{v}^n \Delta t^n, \quad \text{(A.7)}$$

where the first three terms are the solution of the homogeneous part of system (31). $\mathbf{C}^m_1$ and $\mathbf{C}^m_2$ are given by:

$$\mathbf{C}^m_1 = \mathbf{u}^m_1 \exp^{\lambda^m_1 \Delta t} \quad \mathbf{C}^m_2 = \mathbf{u}^m_2 \exp^{\lambda^m_2 \Delta t} \quad \text{(A.8)}$$

or

$$\begin{aligned}
\mathbf{C}^m_1 &= \exp^{\lambda^m_r \Delta t}[\mathbf{u}^m_r \cos(\lambda^m_i \Delta t) - \mathbf{u}^m_i \sin(\lambda^m_i \Delta t)], \\
\mathbf{C}^m_2 &= \exp^{\lambda^m_r \Delta t}[\mathbf{u}^m_r \sin(\lambda^m_i \Delta t) + \mathbf{u}^m_i \cos(\lambda^m_i \Delta t)]
\end{aligned} \quad \text{(A.9, a)}$$

and

$$\mathbf{C}^m_3 = \exp^{\lambda^m_3 \Delta t} \mathbf{u}^m_3. \quad \text{(A.9, b)}$$

Vectors $\mathbf{v}^i$ ($i = 0, 1, 2$) can be computed by comparing terms in the polynomial part of system (31) with the same time exponent. This leads to the sequential solution of the following linear systems:

$$\begin{aligned}
\mathbf{A}^m \mathbf{v}^2 &= -\mathbf{b}^2 \\
\mathbf{A}^m \mathbf{v}^1 &= -\mathbf{b}^1 + 2\mathbf{v}^2 \\
\mathbf{A}^m \mathbf{v}^0 &= -\mathbf{b}^0 + \mathbf{v}^1,
\end{aligned} \quad \text{(A.10)}$$

Coefficients α_1, α_2 and α_3 are computed by forcing the solution of system (31) to honor the initial concentration values at the three nodes of the element, according to the system:

$$\begin{aligned}
\mathbf{C}^m_0 &= \alpha_1 \mathbf{u}^m_1 + \alpha_2 \mathbf{u}^m_2 + \alpha_3 \mathbf{u}^m_3 + \mathbf{v}^0 \quad \text{or} \quad \mathbf{C}^m_0 \\
&= \alpha_1 \mathbf{u}^m_r + \alpha_2 \mathbf{u}^m_i + \alpha_3 \mathbf{u}^m_3 + \mathbf{v}^0,
\end{aligned} \quad \text{(A.11)}$$

where $\mathbf{C}^m_0$ is the vector of the initial nodal concentrations.

Once the ODEs system (31) is solved for element T_m, polynomial coefficients in Eq. (32) can be set in order to honour the computed initial and final values, as well as to match the mean in time value of each polynomial approximation with the one computed by the analytical solution, that is:

$$\begin{aligned}
&\xi^{m,0}_j = C^m_j(t^k), \quad \xi^{m,0}_j + \xi^{m,1}_j \Delta t + \xi^{m,2}_j \Delta t^2 = C^m_j(t^{k+1/2}), \\
&\xi^{m,0}_j + \xi^{m,1}_j \frac{\Delta t}{2} + \xi^{m,2}_j \frac{\Delta t^2}{3} = \bar{\xi}^m_j \quad j = 1, 2, 3,
\end{aligned} \quad \text{(A.12)}$$

where $\bar{\xi}^m_j$ is obtained by solving the following linear system (A.12), given by the 0th and 1st order moment balance equations:

$$\begin{aligned}
&\begin{pmatrix}
-\sum_{j=1,3} \frac{1-\delta_i}{|T_m|} \int_{l_j} \phi^m_j \bar{\xi}^m_j(r_j) dl - \frac{1}{3} \sum_{j=1,3} \widehat{\omega_e} \, \widehat{\lambda_e} \, \bar{\xi}^m_j \\
\frac{|T_m| q^m_{x_1}}{3} \sum_{j=1,3} \bar{\xi}^m_j - \sum_{j=1,3} (1-\delta_j) \int_{l^m_j} \phi^m_j \bar{\xi}^m_j(r_j)(x_1 - x^m_{1,G}) dl \\
\frac{|T_m| q^m_{x_2}}{3} \sum_{j=1,3} \bar{\xi}^m_j - \sum_{j=1,3} (1-\delta_j) \int_{l^m_j} \phi^m_j \bar{\xi}^m_j(r_j)(x_2 - x^m_{2,G}) dl
\end{pmatrix} \\
&= \mathbf{B}^m \frac{\widehat{\omega_m}}{\Delta t} \begin{pmatrix}
C^m_1(t^{k+1/2}) - C^m_1(t^k) \\
C^m_2(t^{k+1/2}) - C^m_2(t^k) \\
C^m_3(t^{k+1/2}) - C^m_3(t^k)
\end{pmatrix} \\
&- \begin{pmatrix}
\sum_{j=1,3} \frac{\delta_i}{|T_m|} \int_{l^e_{jm}} \phi^e_{jm} \bar{\xi}^e_{jm}(r_{jm}) dl + \overline{f^m_C} \\
\sum_{j=1,3} \delta_i \int_{l^e_{jm}} \phi^e_{jm} \bar{\xi}^e_{jm}(r_{jm})(x_1 - x^m_{1,G}) dl \\
\sum_{j=1,3} \delta_i \int_{l^e_{jm}} \phi^e_{jm} \bar{\xi}^e_{jm}(r_{jm})(x_2 - x^m_{2,G}) dl
\end{pmatrix}. \quad \text{(A.13)}
\end{aligned}$$

The linear integrals on the l.h.s. of Eq. (A.13) are the mean (in time) values of the leaving mass and moment fluxes and linear concentration profile $\bar{\xi}^m_j(r_j)$ in side j is computed as function of the unknown mean concentration value at point with abscissa r_j on side j with leaving flux. $\bar{\xi}^m_j(r_j)$ is function of the unknowns mean nodal values on side j. Term $\frac{|T_m| q^m_{x_{1(2)}}}{3} \sum_{j=1,3} \bar{\xi}^m_j$ is the variation of the 1st order moment due to the movement of the centroid in $x_{1(2)}$ direction. The first term on the r. h. s. is the mean (in time) value of the mass and moment change. The linear integrals in the second term on the r. h. s. are the mean (in time) values of the incoming mass and x_1 and x_2 1st order moment fluxes; these are function of the mean concentration $\bar{\xi}^e_{jm}(r_{jm})$ at any point on side jm with abscissa r_{jm}. $\bar{\xi}^e_{jm}(r_{jm})$ can be computed according to both mean nodal concentration values of side jm.

Appendix B. Solution of the correction transport problem

Define:

$$\mathbf{t}_{i,ip} = \frac{\mathbf{r}_{i,ip}}{|\mathbf{r}_{i,ip}|}, \quad \mathbf{t}_{i,im} = \frac{\mathbf{r}_{i,im}}{|\mathbf{r}_{i,im}|}, \quad \text{(B.1)}$$

the two unit vectors parallel to sides $\mathbf{r}_{i,ip}$ and $\mathbf{r}_{i,im}$ (see Fig. 5(a)). Flux coefficient across $|P_{i,ip} \tilde{c}_{T_m}|$ due to a unitary difference between C values in ip and i is computed as [3]:

$$F^{T_m}_{i,ip} = -\left[\mathbf{D} \mathbf{t}_{i,ip} \frac{(C_{ip} - C_i)}{|\mathbf{r}_{i,ip}|} \wedge (\mathbf{x}^{T_m}_c - \mathbf{x}_{i,ip})\right] \frac{1}{|C_{ip} - C_i|}. \quad \text{(B.2, a)}$$

Similarly, flux coefficient across $|P_{i,im} \tilde{c}_{T_m}|$ due to a unitary difference of C values in nodes im and i is:

$$F^{T_m}_{i,im} = -\left[\mathbf{D} \mathbf{t}_{i,im} \frac{(C_{im} - C_i)}{|\mathbf{r}_{i,im}|} \wedge (\mathbf{x}_{i,im} - \mathbf{x}^{T_m}_c)\right] \frac{1}{|C_i - C_{im}|}, \quad \text{(B.2, b)}$$

where the Euclidean norm of $\mathbf{r}_{i,ip}$ ($r_{i,im}$) is also the distance between nodes i and ip (im). Finally, coefficients $F^{T_m}_{i,ip}$ and $F^{T_m}_{i,im}$ can be computed as:

$$F^{T_m}_{i,ip} = -\mathbf{D}(\mathbf{x}_{ip} - \mathbf{x}_i) \wedge (\mathbf{x}^{T_m}_c - \mathbf{x}_{i,ip}) \frac{1}{|\mathbf{r}_{i,ip}|^2} \quad \text{(B.3, a)}$$

$$F^{T_m}_{i,im} = -\mathbf{D}(\mathbf{x}_i - \mathbf{x}_{im}) \wedge (\mathbf{x}^{T_m}_c - \mathbf{x}_{i,im}) \frac{1}{|\mathbf{r}_{i,im}|^2}, \quad \text{(B.3, b)}$$

with the symbols specified in Section 4.2. The extra-diagonal coefficient $F_{i,im}$ of the stiffness matrix of the resolving system is given by the sum of the unitary coefficients across $|P_{i,im}\tilde{c}_{T_m}|$ and $|P_{i,ip}\tilde{c}_{T_e}|$:

$$F_{i,im} = F_{i,im}^{T_m} + F_{im,i}^{T_e}, \tag{B.4}$$

(coefficients $F_{i,im}^{T_m}$ and $F_{im,i}^{T_e}$ are given in Eqs. (B.3)). Eq. (B.4) can be written as:

$$F_{i,im} = -\mathbf{D}^{T_m}\left(\mathbf{x}_i - \mathbf{x}_{im}\right) \wedge \left(\mathbf{x}_c^{T_m} - \mathbf{x}_{i,im}\right)\frac{1}{|\mathbf{r}_{i,im}|^2} - \mathbf{D}^{T_e}\left(\mathbf{x}_{im} - \mathbf{x}_i\right)$$
$$\wedge \left(\mathbf{x}_c^{T_e} - \mathbf{x}_{i,im}\right)\frac{1}{|\mathbf{r}_{i,im}|^2} \tag{B.5}$$

and $\mathbf{D}^{T_{m(e)}}$ is the diffusive tensor for element $T_{m(e)}$. Eq. (B.5) can then be written as:

$$F_{i,im} = -\frac{\left(d_{i,im}^{T_m}\tilde{c}_{i,im}^{T_m}\sin\theta_{T_m} + d_{im,i}^{T_e}\tilde{c}_{im,i}^{T_e}\sin\theta_{T_e}\right)}{|\mathbf{r}_{i,im}|^2}, \tag{B.6}$$

where $\tilde{c}_{p,pm}^{T_q}$ and $d_{p,pm}^{T_q}$ are defined in Eqs. (42) and (40), θ_{T_q} is defined in Section 4.2. Eq. (B.6) is the same as Eq. (39).

References

[1] Aricò C, Tucciarelli T. MAST solution of advection problems in irrotational flow fields. Adv Water Resour 2007;30:665–85.

[2] Aricò C, Sinagra M, Begnudelli L, Tucciarelli T. MAST-2D diffusive model for flood prediction on domains with triangular Delaunay unstructured meshes. Adv Water Resour 2011;34:1427–49.

[3] Aricò C, Tucciarelli T. Monotonic solution of heterogeneous anisotropic diffusion problems. J Comput Phys 2012, (submitted for publication).

[4] Bascià A, Tucciarelli T. An explicit unconditionally stable numerical solution of the advection problem in irrotational flow fields. Water Resour Res 2004; 40(6):W06501.

[5] Bear J. Dynamics of fluids in porous media. New York: Dover; 1972.

[6] Bear J. Hydraulics of groundwater. New York: McGraw-Hill; 1979.

[7] Bergamaschi L, Putti M. Mixed finite elements and newton-type linearization for the solution of Richards' equation. Int J Numer Methods Eng 1999;45: 1025–46.

[8] Bernard-Michel G, Le Potier C, Beccantini A, Gounand S, Chraibi M. The Andra Couplex 1 test case: comparison between finite-element, mixed hybrid finite element and finite volume element discretizations. Comput Geosci 2004;8:187–201.

[9] Bourgeat A, Kern M, Schumacher S, Talandier J. The COPLEX test cases: nuclear waste disposal simulation. Comput Geosci 2004;8:83–98.

[10] Casulli V. Eulerian–Lagrangian methods for hyperbolic and convection dominated parabolic problems. Computational Methods for Nonlinear Problems. Swansea: Pineridge; 1987. pp. 239–269.

[11] Celia MA, Bouloutas ET, Zarba RL. A general mass-conservative numerical solution for the unsaturated flow equation. Water Resour Res 1990;26: 1483–96.

[12] Celia MA, Russell TF, Herrera I, Ewing RE. An Eulerian–Lagrangian localized adjoint method for the advection–diffusion equation. Adv Water Resour 1990;13:187–206.

[13] Chavent G, Younes A, Ackerer P. On the finite volume reformulation of the mixed finite element method for elliptic and parabolic PDE on triangles. Compu Methods Appl Mech Eng 2003;192:655–82.

[14] Dawson CN. Godunov-mixed methods for advective flow problems in one space dimension. SIAM J Numer Anal 1991;28(5):1282–309.

[15] Dawson CN. Godunov-mixed methods for advection–diffusion equations in multidimension. SIAM J Numer Anal 1993;30(5):1315–32.

[16] Diersch H-JG, Kolditz O. Variable-density flow and transport in porous media: approaches and challenges. Adv Water Resour 2002;25:899–944.

[17] Forsyth PA. A control volume finite element approach to NAPL groundwater contamination. SIAM J Sci Stat Comput 1991;12:1029–57.

[18] Gallo C, Manzini G. A mixed finite element/finite volume approach for solving biodegradation transport in groundwater. Int J Numer Methods Fluids 1998;26(5):533–56.

[19] Gallo C, Manzini G. A fully coupled numerical model for two-phase flow with contaminant transport and biodegradation kinetics. Commun Numer Methods Eng 2001;17(5):325–36.

[20] Gao Z, Wu J. A linearity-preserving cell-centered scheme for the heterogeneous and anisotropic diffusion equations on general meshes. Int J Numer Methods Fluids 2011;67(12):2157–83.

[21] Havu V. An analysis of asymptotic consistency error in a parameter dependent model problem. Calcolo 2003;40(2):121–30.

[22] Havu V, Pitkäranta J. An analysis of finite element locking in a parameter dependent model problem. Numer Math 2001;89(4):691–714.

[23] Healy RW, Russel TF. Solution of the advection–dispersion equation in two dimensions by a finite-volume Eulerian–Lagrangian localized adjoint method. Adv Water Resour 1998;21(1):11–26.

[24] Herbin R, Hubert F. Benchmark on discretization schemes for anisotropic diffusion problems on general grids. In: Finite volumes for complex applications V. London: ISTE; 2008. p. 659–92.

[25] Hererra PA, Massabò M, Beckie RD. A meshless method to simulate solute transport in heterogeneous porous media. Adv Water Resour 2009;32(3): 413–29.

[26] Hoteit H, Erhel J, Mosé R, Philippe B, Ackerer P. Numerical reliability for mixed methods applied to flow problems in porous media. Comput Geosci 2002;6: 161–94.

[27] Joe B. Delaunay triangular meshes in convex polygons. SIAM J Sci Stat Comput 1986;7:514–39.

[28] Li X, Huang W. An anisotropic mesh adaptation method for the finite element solution of heterogeneous anisotropic diffusion problems. J Comput Phys 2010;229(21):8072–94.

[29] Mazzia A, Bergamaschi L, Dawson CN, Putti M. Godunov mixed methods on triangular grids for advection–dispersion equations. Comput Geosci 2002;6(2):123–39.

[30] Mazzia A, Manzini G, Putti M. Bad behaviour of Godunov mixed methods for strongly anisotropic advection–dispersion equations. J Comput Phys 2011;230(23):8410–26.

[31] Neumann SP. A Eulerian–Lagrangian numerical scheme for the dispersion convection equation using conjugate space time grids. J Comput Phys 1981;41: 270–94.

[32] Putti M, Cordes C. Finite element approximation of the diffusion operator on tetrahedral. SIAM J Sci Comput 1998;19(4):1154–68.

[33] Raviart PA, Thomas JA. A mixed finite element method for second order elliptic problems. In: Mathematical aspects of finite element method. Lecture notes in mathematics, 606. New York: Springer; 1977. p. 292–315.

[34] Younes A, Ackerer P, Chavent G. From mixed finite elements to finite volumes for elliptic PDE in 2 and 3 dimensions. Int J Numer Methods Eng 2004;59: 365–88.

[35] Younes A, Ackerer P, Leheman F. A new mass lumping scheme for the mixed hybrid finite element method. Int J Numer Methods Eng 2006;67:89–107.